NASA/TP-2011-217350

Michigan Orbital DEbris Survey Telescope Observations of the Geosynchronous Orbital Debris Environment

Observing Years: 2007–2009

K. J. Abercromby[1], P. Seitzer[2], H. M. Cowardin[3], E. S. Barker[4], and M. J. Matney[5]

[1]California Polytechnic State University, San Luis Obispo
Department of Aerospace Engineering
San Luis Obispo, CA 93407

[2]University of Michigan
Department of Astronomy
Ann Arbor, MI 48109-1042

[3]ESC Group/Jacobs
Houston, TX 77058

[4]LZ Technology
Houston, TX 77058

[5]National Aeronautics and Space Administration
Johnson Space Center
Houston, TX 77058

National Aeronautics and
Space Administration

Johnson Space Center
Houston, TX 77058

September 2011

THE NASA STI PROGRAM OFFICE . . . IN PROFILE

Since its founding, NASA has been dedicated to the advancement of aeronautics and space science. The NASA Scientific and Technical Information (STI) Program Office plays a key part in helping NASA maintain this important role.

The NASA STI Program Office is operated by Langley Research Center, the lead center for NASA's scientific and technical information. The NASA STI Program Office provides access to the NASA STI Database, the largest collection of aeronautical and space science STI in the world. The Program Office is also NASA's institutional mechanism for disseminating the results of its research and development activities. These results are published by NASA in the NASA STI Report Series, which includes the following report types:

- TECHNICAL PUBLICATION. Reports of completed research or a major significant phase of research that present the results of NASA programs and include extensive data or theoretical analysis. Includes compilations of significant scientific and technical data and information deemed to be of continuing reference value. NASA's counterpart of peer-reviewed formal professional papers but has less stringent limitations on manuscript length and extent of graphic presentations.
- TECHNICAL MEMORANDUM. Scientific and technical findings that are preliminary or of specialized interest, eg, quick release reports, working papers, and bibliographies that contain minimal annotation. Does not contain extensive analysis.
- CONTRACTOR REPORT. Scientific and technical findings by NASA-sponsored contractors and grantees.
- CONFERENCE PUBLICATION. Collected papers from scientific and technical conferences, symposia, seminars, or other meetings sponsored or cosponsored by NASA.
- SPECIAL PUBLICATION. Scientific, technical, or historical information from NASA programs, projects, and mission, often concerned with subjects having substantial public interest.
- TECHNICAL TRANSLATION. English-language translations of foreign scientific and technical material pertinent to NASA's mission.

Specialized services that complement the STI Program Office's diverse offerings include creating custom thesauri, building customized databases, organizing and publishing research results . . . even providing videos.

For more information about the NASA STI Program Office, see the following:

- Access the NASA STI Program Home Page at http://www.sti.nasa.gov
- E-mail your question via the Internet to help@sti.nasa.gov
- Fax your question to the NASA Access Help Desk at (301) 621-0134
- Telephone the NASA Access Help Desk at (301) 621-0390
- Write to:
  NASA Access Help Desk
  NASA Center for AeroSpace Information
  7115 Standard
  Hanover, MD 21076-1320

NASA/TP-2011-217350

Michigan Orbital DEbris Survey Telescope Observations of the Geosynchronous Orbital Debris Environment

Observing Years: 2007–2009

K. J. Abercromby[1], P. Seitzer[2], H. M. Cowardin[3], E. S. Barker[4], and M. J. Matney[5]

[1]California Polytechnic State University, San Luis Obispo
Department of Aerospace Engineering
San Luis Obispo, CA 93407

[2]University of Michigan
Department of Astronomy
Ann Arbor, MI 48109-1042

[3]ESC Group/Jacobs
Houston, TX 77058

[4]LZ Technology
Houston, TX 77058

[5]National Aeronautics and Space Administration
Johnson Space Center
Houston, TX 77058

National Aeronautics and
Space Administration

Johnson Space Center
Houston, TX 77058

September 2011

Available from:

NASA Center for AeroSpace Information
7115 Standard Drive
Hanover, MD 21076-1320
301-621-0390

National Technical Information Service
5285 Port Royal Road
Springfield, VA 22161
703-605-6000

This report is also available in electronic form at http://ston.jsc.nasa.gov/collections/TRS/

Contents

Figures

Tables

Acronyms

ACO	assumed circular orbit
CCD	Charge-Coupled Device
CDT	CCD Debris Telescope
CIS	Commonwealth of Independent States
CT	correlated target
CTIO	Cerro Tololo Inter-American Observatory
CY	calendar year
DEC	declination
DOY	day of year
F	functional [used only in figure callouts]
FOV	field of view
FWHM	full width at half maximum
GEO	geosynchronous orbit
GEODSS	Ground-based Electro-Optical Deep Space Surveillance
HA	hour angle
INC	inclination
JSC	Johnson Space Center
LST	local sidereal time
MODEST	Michigan Orbital DEbris Survey Telescope
NF	nonfunctional [used only in figure callouts]
OH	oxygen-hydrogen-bond emission
RA	right ascension
RAAN	right ascension of ascending node
RMS	root mean square
S/N	signal to noise
SATRAK	satellite missile tracking program
SGP	Simplified General Perturbation code
SSN	Space Surveillance Network
TDI	time delay integration
TLE	two-line element
UCT	uncorrelated target
UT	universal time

Executive Summary

NASA uses the Michigan Orbital DEbris Survey Telescope (MODEST), the University of Michigan's 0.61-m aperture Curtis-Schmidt telescope at the Cerro Tololo Inter-American Observatory in Chile, to help characterize the debris environment in geosynchronous orbit; this began in February 2001 and continues to the present day. Detected objects that are found to be on the U.S. Space Surveillance Network cataloged objects list are termed correlated targets (CTs), while those not found on the list are called uncorrelated targets (UCTs).

This Johnson Space Center report provides details of observational and data-reduction processes for the entire MODEST dataset acquired in calendar years (CYs) 2007, 2008, and 2009. Specifically, this report describes the collection and analysis of 36 nights of data collected in CY 2007, 43 nights of data collected in CY 2008, and 43 nights of data collected in CY 2009.

MODEST is equipped with a 2048×2048-pixel charged coupled device camera with a 1.3 by 1.3 deg field of view. This system is capable of detecting objects fainter than 18^{th} magnitude (R filter) using a 5-s integration. This corresponds to a 20-cm diameter, 0.175-albedo object at 36,000 km altitude assuming a diffuse Lambertian phase function. The average number of detections each night over all 3 years was 26. The percentage of this number that represented the UCT population ranged from 34% to 18%, depending on the observing strategy and the field center location.

Due to the short orbital arc over which observations are made, the eccentricity of the object's orbit is extremely difficult to measure accurately. Therefore, a circular orbit was assumed when calculating the orbital elements. A comparison of the measured inclination (INC), right ascension of ascending node (RAAN), and mean motion to the quantities for CTs from the U.S. Space Surveillance Network shows acceptable errors. This analysis lends credibility to the determination of the UCT orbital distributions.

Figure 1 shows the size distribution of 3,143 objects detected in the data processed for CYs 2007, 2008, and 2009. The actual peak of the absolute magnitude distribution for the functional correlated targets is 10^{th} magnitude, whereas the peak was 11^{th} magnitude in 2002–2003 and 10^{th} magnitude for 2004-2006. An absolute magnitude of 10.5 corresponds to objects with average diameters of 6.3 m, assuming an albedo of 0.175 and a diffuse Lambertian phase function. This result generally agrees with the known sizes of intact satellites. The absolute magnitude distribution for the UCTs is broad, but starts to roll off near 25 cm diameter or 17.5 magnitude. This roll off in the distribution reflects the detection capability of MODEST, not the true nature of the population. The true population is believed to continue at the same slope through fainter magnitudes based on comparisons with the LEO break-up law.

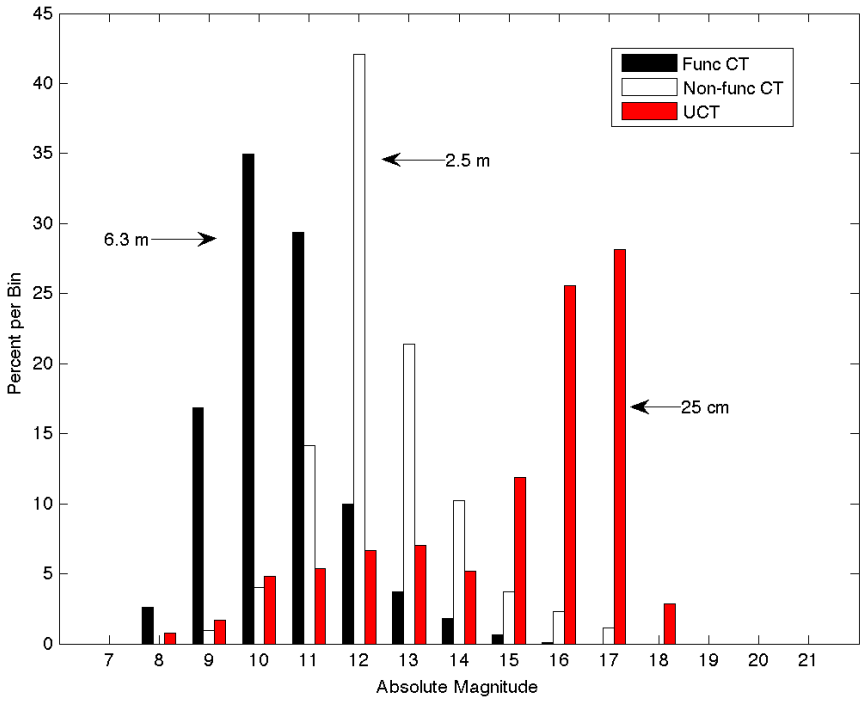

Figure 1. Absolute magnitude and derived size distribution, assuming an albedo of 0.175 and a diffuse Lambertian phase function.

1.0 Introduction

Orbital debris is a concern to all nations that use satellites or launch space vehicles. The debris field scattered near Earth's geosynchronous orbit (GEO) poses a threat to anything residing in or passing through it. To mitigate risk and minimize this environment's expansion, the debris environment must be understood. NASA uses the Michigan Orbital Debris Survey Telescope (MODEST), a University of Michigan-owned 0.61-m aperture Schmidt telescope at the Cerro Tololo Inter-American Observatory (CTIO) in Chile, to help characterize this environment in GEO. The objectives for this survey are to determine the extent and character of debris in GEO, specifically by obtaining distributions for the brightness, inclination (INC), right ascension of ascending node (RAAN), and mean motion for the debris.

2.0 Background

The GEO environment's debris population has a high potential for collision with operational satellites due to the extremely long lifetimes of debris and satellites. Space-faring nations have been placing satellites into GEO since the mid- to late-1960s. Along with operational satellites, debris has been placed into GEO. This debris consists of dead satellites, rocket body upper stages, deployment hardware, small debris, etc. To date, two breakups have been reported in GEO. The first of these, the 1978 breakup of an EKRAN 2 satellite, Space Surveillance Network (SSN) 10365, went unreported prior to its identification in 1992 by the Commonwealth of Independent States (CIS).[1] In 1992, a Titan 3C Transtage breakup, SSN 3432,[1,2] produced at least 20 pieces of debris. Ground-based Electro-Optical Deep Space Surveillance (GEODSS) telescopes tracked these objects for a few days after the event; all but eight pieces have been lost.

NASA used the Charged-Coupled Device (CCD) Debris Telescope (CDT), a transportable 32-cm Schmidt telescope, to conduct initial GEO surveys. The CDT was shipped to the Hawaiian island of Maui for a survey of the GEO environment conducted by NASA from 1992 through 1994.[3] Results from the survey indicated that, to a limiting apparent magnitude of 17 (~60 cm in diameter), about 27% of all objects in GEO are debris. The actual debris population must be much larger due to the presence of objects smaller than 60 cm in diameter. NASA moved the CDT to Cloudcroft, NM, for further GEO studies, where data were collected from November 1997 to December 2001. Due to funding issues, the CDT was shut down in December 2001.

The MODEST program benefits from the data collected by the CDT. The CDT determined the rate at which most GEO objects are traveling.

3.0 Observation Overview

3.1 The MODEST System

The MODEST system uses the University of Michigan's Curtis-Schmidt telescope located at the CTIO in Chile. Since February 2001, the telescope has been dedicated to optical studies of orbital debris for NASA's Orbital Debris Program Office at the Johnson Space Center (JSC).

The telescope is a 0.61-m aperture f/3.5 Schmidt of classical design, with a CCD mounted at a Newtonian focus. The CCD is a thinned, backside-illuminated device manufactured by SITe. The format is

2048 × 2048 pixels, each of which is 24 microns square. This provides a 2.318-arc-seconds/pixel sampling and a 1.3×1.3-deg field of view (FOV).

A 5-s exposure through a broad R filter centered at 630 nm and 200 nm wide (full width at half maximum [FWHM]) produces a signal-to-noise (S/N) = 10 on a point source detection of 18th R magnitude under typical dark sky conditions at Tololo.

A picture of the MODEST telescope is shown in Figure 2.

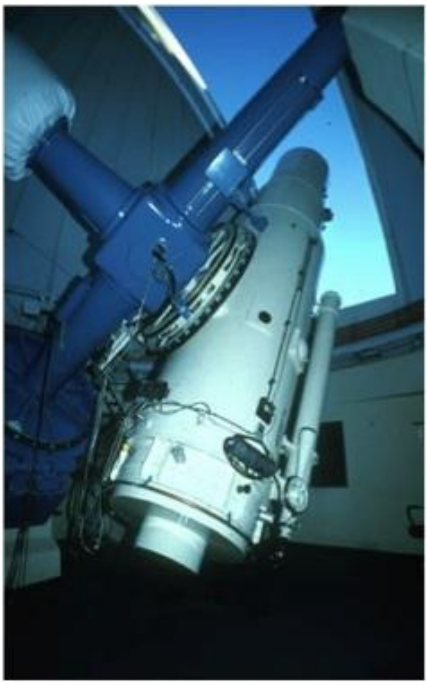

Figure 2. The MODEST telescope.

3.2 Search Strategy

Numerous studies[4,5] provide compelling arguments that most uncontrolled debris objects in GEO should be at INCs less than or equal to 15°. Orbits of uncontrolled GEO objects oscillate around the stable Laplacian plane, which has an INC of 7.5° with respect to the equatorial plane. This oscillation is dominated by the combined effects of the Earth's oblateness (J2 term) and solar and lunar perturbations. The INC oscillation period is about 50 years. During the first 25 years, an uncontrolled object with an initial INC of 0° will gradually increase in INC until its INC has peaked at 15°. During the next 25 years, this same object's INC will gradually decrease until it has returned to its original INC, in this case, 0°, and it will begin its oscillation cycle again. Most uncontrolled objects with a different initial INC will follow the same 50-year pattern of increasing their INC to 15°, decreasing to 0°, and then returning to their original INC. (There are some cases in which the INC will first decrease to 0°.) Depending on the insertion RAAN, an uncontrolled object's oscillation can be out of phase with other objects, although these examples are few.

Figure 3 shows the INC of objects in GEO plotted against their launch date. These data were taken from the element set file as of day 365, year 2003, and plots 2,884 objects. All objects plotted have mean motions of less than 1.1 revs/day. The oldest have already peaked in INC and are now approaching 0° INC again. Figure 4 shows one catalog object's progression in INC over time. This object's INC increased to

15° and is on its way toward decreasing back to 0°. There is also a strong correlation between an object's INC and its RAAN, as illustrated in Figure 5.

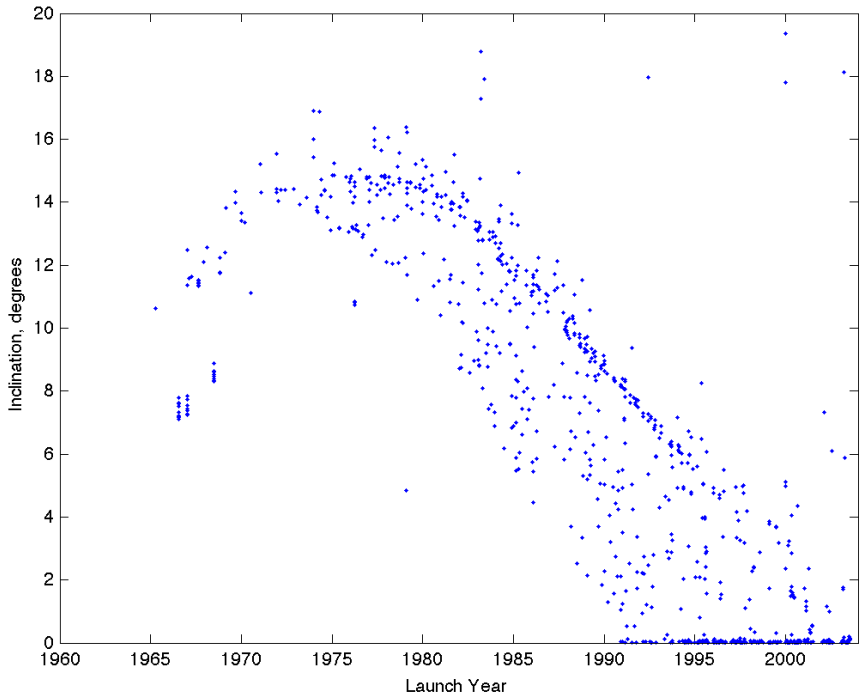

Figure 3. Inclination vs. launch date.

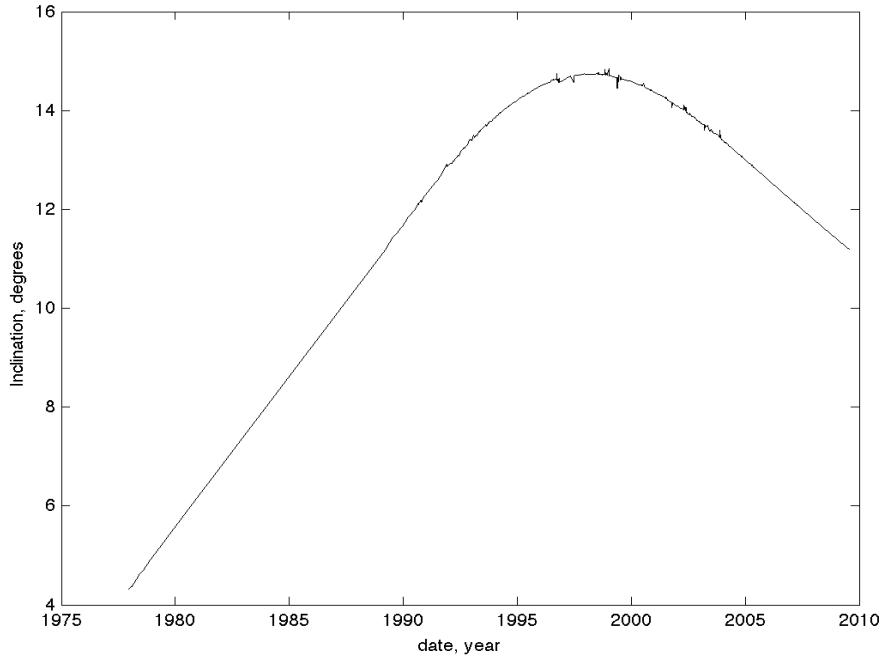

Figure 4. A catalog object showing the date of observation vs. inclination. These data show the progression of INC over time, with the noise being bad data points.

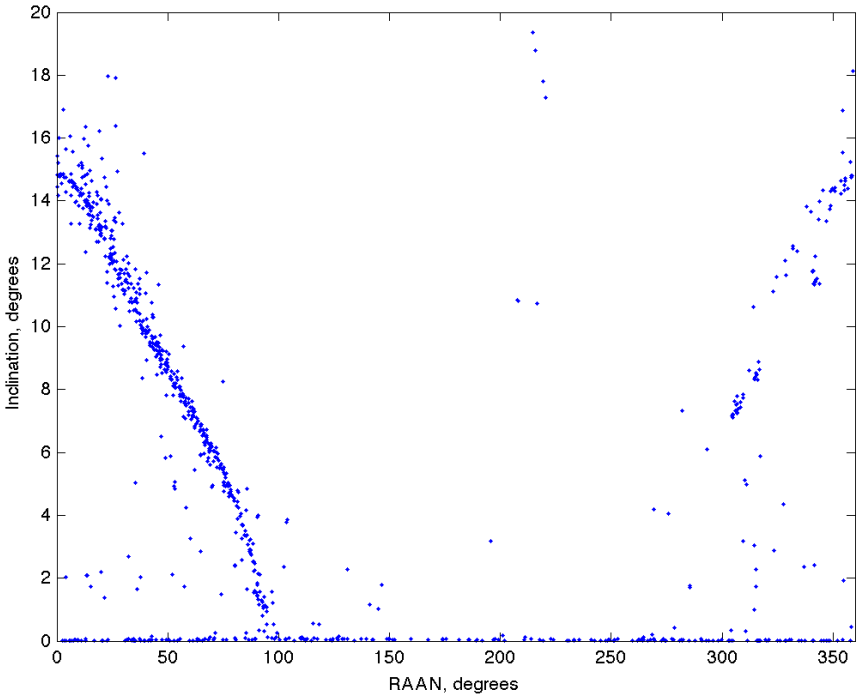

Figure 5. RAAN vs. INC for near-GEO objects.

Figure 6 illustrates the daily motion for a set of objects having mean motions less than 1.1 revs/day and INCs less than 17°. These data are for a given date and time in 2003. Since most orbital debris will be associated with operational satellites, searches need to be made above or below the equator at the appropriate times to maximize the detection rate of the debris. While there may be a few very interesting objects outside of this envelope, most debris will be found near or inside it. As a result of the systematic orientation of the orbital planes, objects with a given INC will be above (or below) the Earth's equator at the same time.

To date, the best way found to represent orbital debris magnitude variations as a function of phase angle is a Lambertian phase function, in which the maximum brightness is observed at the 0° phase angle.[6] To detect the smallest debris possible, it is best to observe them under nearly face-on (small phase angle) solar illumination. This condition is most closely reached for objects near the anti-solar point. Since Earth's shadow projected into space has a finite angular diameter, on the order of 17° at geosynchronous distances, it is impossible to meet the condition of exact face-on illumination (phase angle = 0°).

From MODEST's location, orbital longitudes from 25°W to 135°W can be seen. Each night, MODEST observers determine a specific right ascension (RA) and declination (DEC) that is the closest to the anti-solar point as possible without being in the Earth's shadow. The telescope then stares at that location for the night. However, on nights near the equinoxes when the shadow overlaps the region of interest, two fields are observed by switching locations halfway through the night, with the first half of the night leading the shadow of the Earth and the second half of the night trailing the shadow. All telescope-pointing locations are determined prior to the start of the run. The location of the moon also plays a role as to when observations can occur. As a general rule, observations take place ±1 week around the new moon.

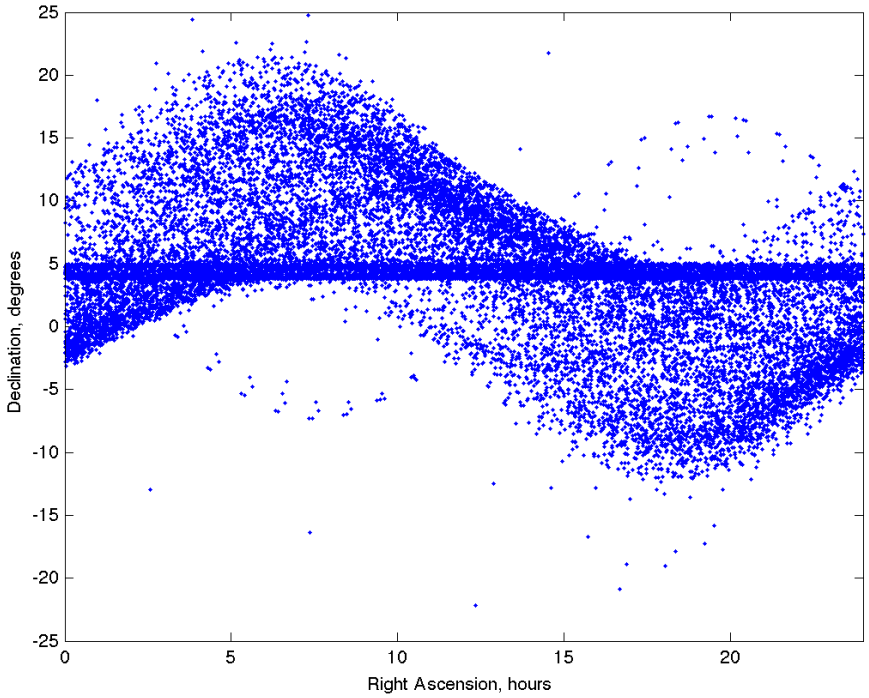

Figure 6. Daily motion for GEO objects (RA vs. DEC) as viewed from CTIO, Chile.

3.3 Data Collection

The telescope tracks the RA and DEC at the sidereal rate. During the 5-s exposure, the charge on the CCD is shifted in reverse so that the objects are seen as a point source and the stars are seen as streaks. This mode is known as time delay integration (TDI). Thus, the system has peak sensitivity to objects with the expected motion of GEO objects. Objects orbiting the Earth can appear as streaks depending on their altitude and INC. These streaks will not have the same length or the same general orientation as the star streaks, making them easy to differentiate from the stars.

The standard exposure time is 5 s with a total time between exposures of 37.9 s. An S/N of 10 corresponds to about an 18^{th}-magnitude (in R) limit for one frame. The frame number, RA, DEC, instrumental magnitude, epoch, observation date, and universal time (UT) are calculated for each detection of each object. The instrumental magnitude is transformed to an R magnitude by observing Landolt standard stars. A broad R filter centered at 630 nm and with FWHM = 200 nm is used for observing. This passband maximizes the final S/N of faint objects by minimizing the signal from the night sky. It also minimizes the scattering of moonlight below 400 nm and OH emissions above 800 nm. Four independent detections are required to consider a source a real object. At the first detection, a computer program (debris finder) determines where the next detection should be for the object given a rate box movement of ±2 arc-second/second in hour angle (HA) and ±5 arc-second/second in DEC. For GEO objects, the total time spent in the FOV is generally 5 min. Figure 7 shows a mosaic of nine frames in a MODEST data set. The object can be seen traveling from the middle left to the upper right as time increases.

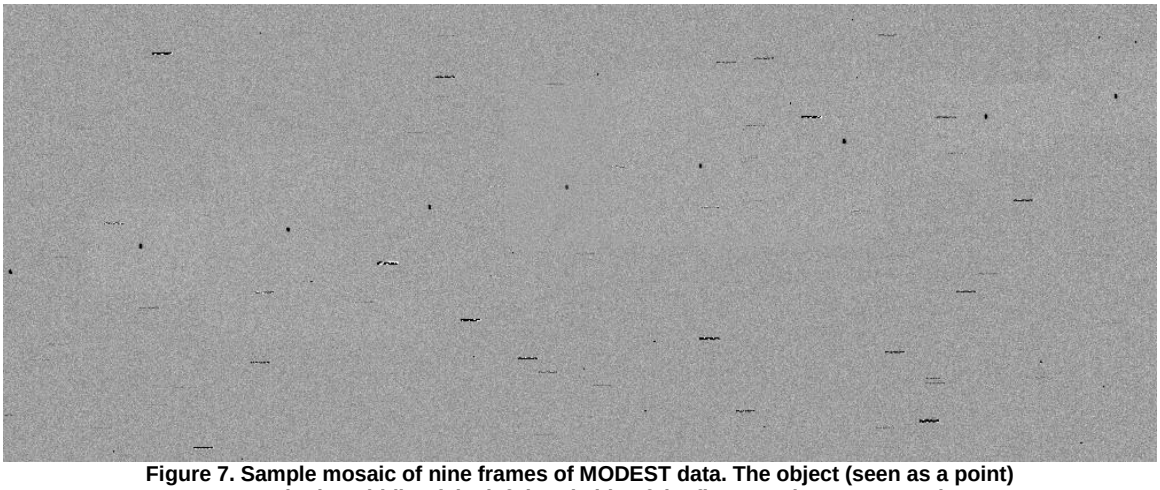

Figure 7. Sample mosaic of nine frames of MODEST data. The object (seen as a point) appears in the middle of the left-hand side of the figure and traverses to the upper right corner. This image is the width (RA) of the FOV but only one-fourth of the height (DEC). The streaks in this image are stars.

In addition to computer detection of objects, a manual review of one night is conducted every 4 months. The manual review consists of two people observing the frames collected in a given night and recording the frames in which objects are seen. These manual observations are then compared to the computer detections to make sure the computer code is catching all the objects it should. In all manual reviews to date, the computer has found 100% of the objects it should, so extreme confidence is established in the ability to find objects that fall within the rate box.

3.4 Data Processing

A real-time data reduction pipeline has been implemented at MODEST that performs the following steps:

- Remove the instrumental signature on each image. This involves subtracting the bias over-scan from each amplifier section, subtracting a master bias to remove low-level bias structure, and dividing by a normalized flat field to remove pixel-to-pixel sensitivity variations.

- Find potential debris candidates, which are either point sources or short streaks (<10 pixels long). This debris finder is insensitive to the 32-pixel-long star streaks.

At the end of the night, a frame-to-frame correlator is run on the candidate lists from all survey images. The output of this correlator is a list of all potential debris candidates that appear in four or more frames, along with their positions and magnitudes. It is assumed that real objects move linearly through subsequent frames.

A nightly manual review is performed at the telescope of all candidates that have five or less detections. False positives (largely due to cosmic rays and the ends of star streaks) are rejected by the operator. Experience has shown there are no false positives with six or more detections.

3.5 Data Analysis

This section describes the process of converting the lists of observations (date, UT, RA, DEC, and magnitude) from the position files into lists of cataloged objects, both correlated targets (CTs) and uncorrelated targets (UCTs), as well as their derivable orbital parameters.

3.5.1 Correlation of detections

Once the data are received by JSC, the correlation of detections is conducted. For each exposure, the day, year, UT, and the field center of the FOV are determined. Then, using an augmented version of the Simplified General Perturbation code (SGP), the satellite catalog is compared to the RA, DEC, and time of each exposure to determine whether an object might be in the FOV. An attempt to correlate all satellites within a 1° radius of the center of the FOV with any detected object is carried out. The results are then output to a file containing all information for all exposures within a given night. Appendix C lists a subset of the file. The program is written with a larger FOV than the true one so that, if any pointing errors arise, a possible correlation still can be obtained.

To correlate an object that was predicted to be in the FOV with an object found in a specific frame, a missed distance is calculated. Missed distance is defined as the absolute value of the squared difference between the observed and the predicted RA and DEC positions. A nightly offset, calculated by taking the average value of the missed distance, is subtracted from the missed distance. Epoch dates (age of an element set) are known to impact the accuracy of where an object is predicted vs. where it is actually located on a given night. This missed distance is not expected to change dramatically as the accuracy of the catalog from year-to-year stays consistent.

If the missed distance is within 0.025°, the software counts the object as a CT. If an object in the FOV cannot be correlated to an object in the catalog, that object is labeled as a UCT. If an object is predicted to be in the FOV but is not seen, it is termed a "no-see." Each correlation is inspected by hand and an override of a computer correlation or non-correlation is possible. On average, 10% of the correlations are done by hand while the computer correlates the remaining 90% of the objects. At times, more than one correlated target in the FOV is within close proximity. In these cases, since the correlation is conducted solely on missed distance, hand correlations are often conducted to ensure that the correct object is associated with the correct SSN.

3.5.2 Orbital elements calculation

The orbit fit program uses a multidimensional simplex optimization routine to fit an orbit to the observations.[7] The observations consist of a series of time-tagged RA and DEC points. The optimization routine finds an orbit that, when propagated to a state vector at the times of individual observations, would appear in the correct positions as viewed from the telescope (with Earth rotation and telescope location included). The parameter to be optimized is the angular distance (averaged over the number of unique observations) between the predicted positions and the computed positions.

Standard Kepler orbital elements tend to be very poor-fitting parameters, especially for orbits with near-zero inclinations and low eccentricities (e.g., GEO orbits) in which elements such as ascending node and argument of perigee become ill-defined. However, an ideal one-to-one conversion exists between any ideal Kepler orbit and a state vector (both referenced to the same epoch). State vectors are attractive candidates for fitting an orbit because they can be varied smoothly without any ill-defined points, at least over a wide range of possible values.

However, using an ideal Kepler orbit may be inadequate for actual orbit fitting. It is useful to include at least the most basic of perturbing terms for realistic orbit predictions. This is accomplished by using the SGP propagator,[8] which includes estimates of the effects of the J_2 term in the Earth's geopotential. The input for SGP is a two-line element (TLE) set that has the same form as classical Kepler orbital elements.

The fitting procedure varies the pseudo-state-vector parameters (defined at a reference epoch for that observation), which are converted directly to Keplerian orbital elements. This Kepler orbit is then treated as the elements of a TLE appropriate for the SGP subroutine. SGP then delivers position predictions at

each of the observation times for that orbit, and these positions are compared to those actually measured until a best-fit solution is achieved. Only the TLE orbit that produced the optimized fit is recorded.

In general, short-arc data are of insufficient quality to compute an accurate orbit eccentricity. However, by penalizing any eccentricity above zero in the optimization portion of the code, a circular-orbit solution can be found.

3.5.3 Comparison of derived orbital quantities with orbital parameters of known objects

The accuracy of the orbital parameters, mean motion, INC, and RAAN for debris can be inferred from the observations of CTs. The error seen in the orbital parameter is due largely to departures from the circular orbit approximation used to calculate the orbital element. In this report, assumed circular orbit (ACO) is the term that describes the orbital element derived from the assumption of a circular orbit. In a similar fashion, the terms "known elements" or "SATRAK [Satellite Tracking (Government owned propagator)] elements" are used interchangeably for elements obtained from cataloged TLE sets. In this report, the terms "inferred" and "known" are used most of the time when discussing data stemming from SATRAK or TLEs.

The viewing geometry for computing the orbit of an object that passes through the FOV is illustrated in Figure 8. The rectangular geocentric equatorial coordinate system is used. The X-axis points in the direction of the vernal equinox, the Y-axis lies in the plane of the equator and points towards longitude 90°, and the Z-axis points towards the celestial north pole. Both the orbital INC, i, and the RAAN can be calculated using the spherical triangles in Figure 8. From the spherical triangle defined by points A – the RAAN; B – the sub-Earth satellite position; and P – the Earth's pole,

$$i = \cos^{-1}[\sin(\mathrm{CBA})\cos(\mathrm{BC})]$$

$$\Delta\lambda = \sin^{-1}[\tan(\mathrm{BC})/\tan(i)]$$

$$\mathrm{RAAN} = \mathrm{LST} + \Delta\lambda$$

where CBA is the angle at which the object crosses the FOV, BC is the sub-satellite latitude, $\Delta\lambda$ (angle CA) is the longitude difference between the sub-satellite longitude and the orbit's ascending node, and LST is the local sidereal time. The proper quadrant for the longitude difference can be determined by inspection. A reasonable estimate of an observed debris object's altitude can be obtained from the distance the object moves along the arc AB during the exposure sequence and by assuming that the object is in a circular orbit. The mean motion can be determined from the known altitude.

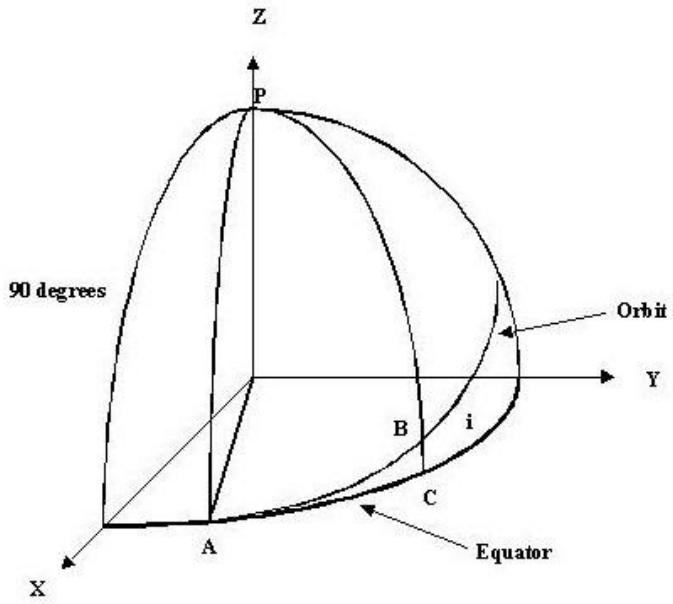

Figure 8. Geometry for computing orbital parameters.

Errors associated with determining the orbital parameters are dependent on the time span over which the observations were obtained, the INC of the orbit, the eccentricity of the orbit, and the pixel size of the CCD.

The root mean square (RMS) of the error is calculated for most of the elements using the calculated element and the TLE element for the CT objects. In addition, for some elements, the category of CT is further broken into functional and nonfunctional objects. The distinction is whether or not the object is believed to be station-kept. Station-kept is defined as those objects that are allowed to drift in the north-south direction but not in the east-west direction. If an object is station-kept, it is called a functional CT; if not, that object is termed a nonfunctional object. There are two reasons for this distinction. First, it is believed that nonfunctional objects should show similar characteristics to orbital debris, thus giving a better estimate of the imposed error on the determination of the orbit. Second, it is possible that a maneuver occurred with a functional object after the TLE was published and before the object was observed. If this is the case, the TLE and the calculated element would show differences that are not errors in the process of calculating the orbit but rather, show that the object is no longer in the same orbit. However rare a case like this may be, it should be considered.

3.5.3.1 Inclination

The inclination of the orbit is the least error-prone of the elements calculated for most objects. The RMS error for INC is shown in Table 1, categorized by calendar year (CY). For these data, there are 332 functional and 281 nonfunctional objects in 2007; 192 functional and 376 nonfunctional objects in 2008; and 818 functional and 310 nonfunctional objects in 2009. Due to more nights spent observing on the GEO belt in 2009, there is an increase in the number of objects detected from 2007 and 2008. This will be discussed in more detail in Section 4.1. The errors are similar for all years, meaning that regardless of the locations observed, the errors are consistent. The INC RMS error data shown in the table are separated into functional and nonfunctional objects, as well as CY. Functional objects are those that are believed to be actively station-keeping, whereas nonfunctional objects appear not to be station-kept.

Table 1. Inclination Errors for CY 2007, CY 2008, and CY 2009

Types of Error (reported in degrees)	Functional Objects	Nonfunctional Objects
RMS 2007	0.06	0.05
RMS 2008	0.04	0.03
RMS 2009	0.05	0.06

Figure 9 shows the ACO INC vs. predicted INC for both functional and nonfunctional targets. The solid line indicates where the quantities are equal. All 3 years show good agreement, and this was an expected result. Very few objects are seen as outliers in this figure, whereas in previous years some outliers were observed. With the circular orbit assumption, it is understandable that the INC would be off, even slightly, for these objects.

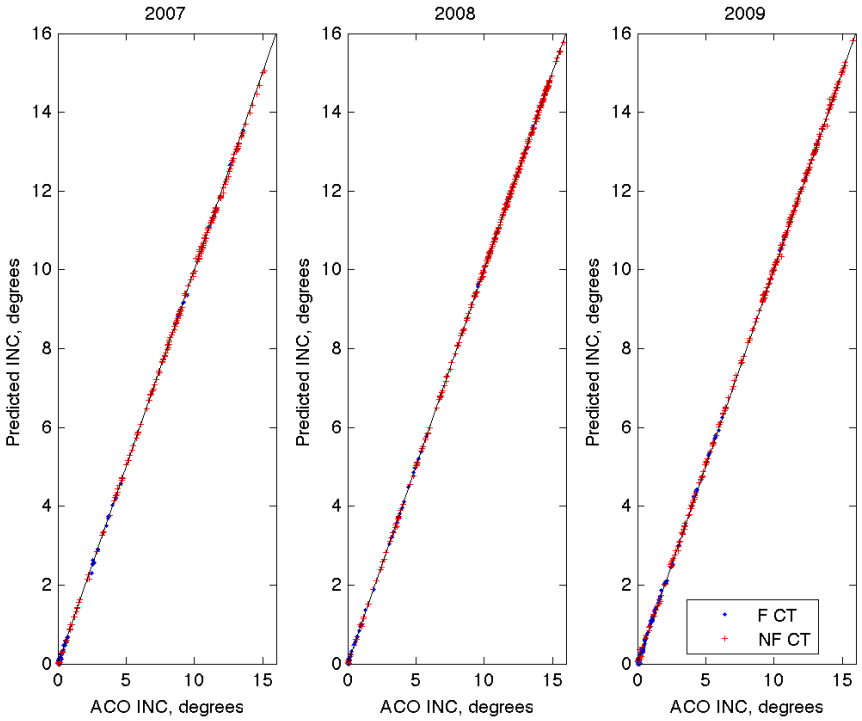

Figure 9. INC comparison for correlated targets separated into functional (F) and nonfunctional (NF) categories. CY 2007 is on the left, CY 2008 is in the center, and CY 2009 is on the right.

In Figure 10, the same data are used; however, the scale is much smaller so that the region less than 1° can be investigated. This change in region is defined as a concise range and will be used throughout the rest of this report. The 2002–2003 MODEST data showed the INC was being underestimated. However, this is not seen as clearly in the 2004-2006 data sets. In this 2007-2009 report, all 3 years show a slight underestimation of INC. Currently, the cause for the underestimation is unknown.

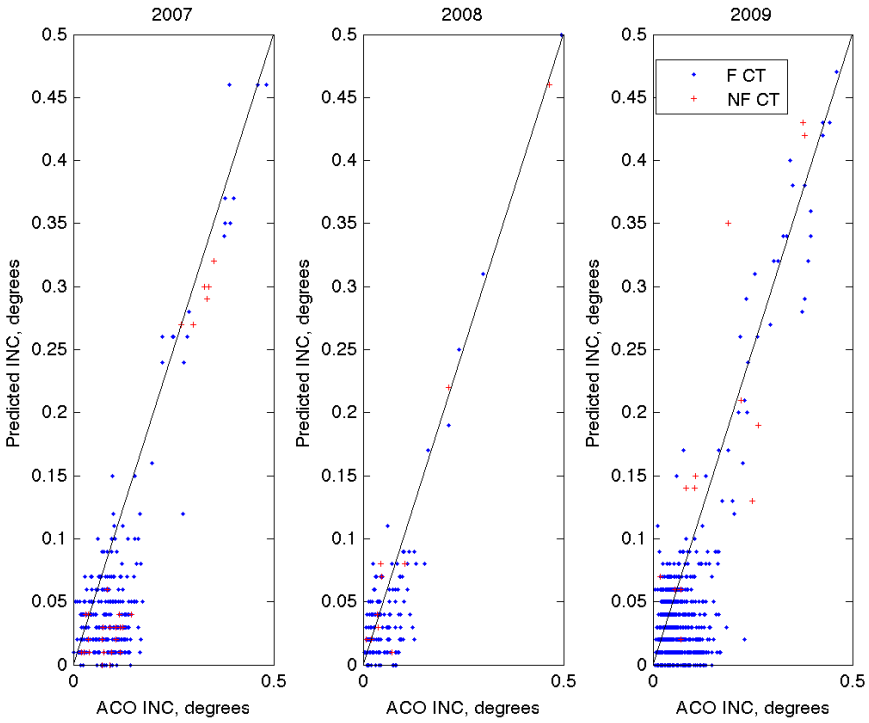

Figure 10. INC comparison for correlated targets separated into functional (F) and nonfunctional (NF) categories, concise range.

An examination of the error in INC vs. the ACO INC was investigated, the results of which are shown in Figure 11 and Figure 12 for both the entire range and a more concise range of inclinations, respectively. This examination was conducted to determine whether large errors were seen at any specific INC or within functional or nonfunctional objects. For all years, functional objects gather near 0°, with all data showing the underestimation of the INC for the functional objects. Nonfunctional objects have an equal spread between over- and underestimation of INC throughout all INC ranges for 2007 and 2008, but the data is overestimated in 2009. Currently, the cause for the overestimation is unknown.

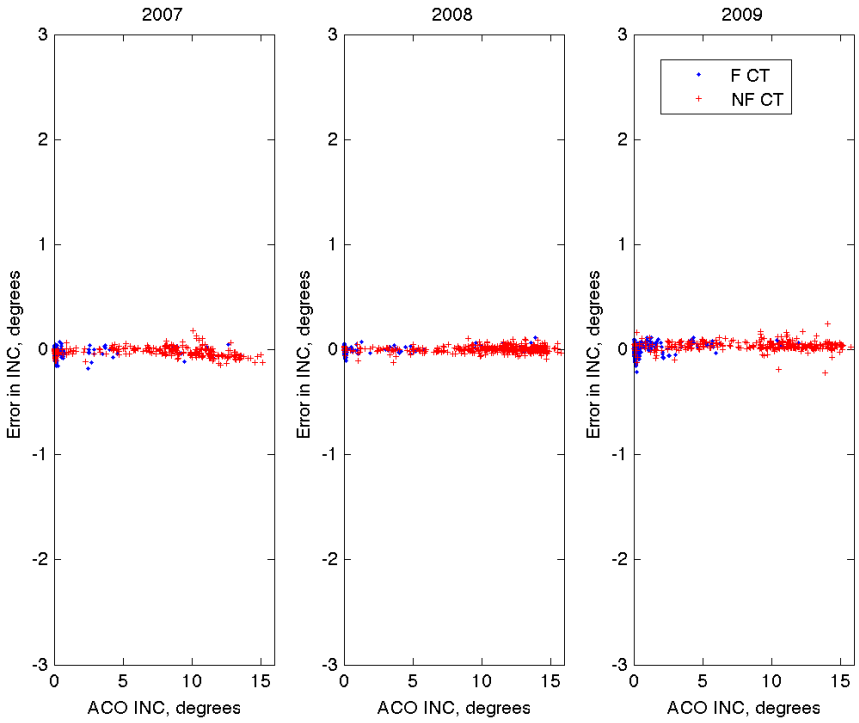

Figure 11. INC error as a function of INC, entire range.

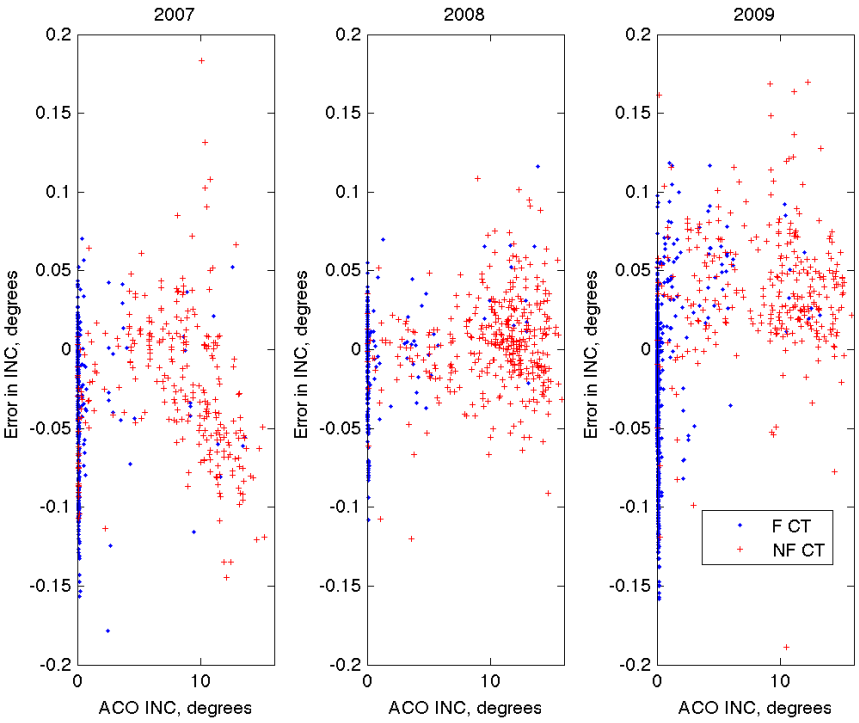

Figure 12. INC error as a function of INC, concise range.

3.5.3.2 Mean Motion Determination

The usual mean motion for geostationary objects is near 1.0027 revs/day. The RMS error for mean motion is shown in Table 2. In this table, there are 332 functional and 281 nonfunctional objects in 2007; 192 functional and 376 nonfunctional objects in 2008; and 818 functional and 310 nonfunctional objects in 2009. The errors are very small for all years, meaning that regardless of the locations observed, the errors are consistent. The errors for nonfunctional objects are slightly larger than those for functional objects, but again, the errors for all cases are very small.

Table 2. Mean Motion Errors

Types of Error	Functional Objects	Nonfunctional Objects
RMS 2007	0.003	0.006
RMS 2008	0.001	0.008
RMS 2009	0.002	0.010

The data for mean motion are plotted in a similar fashion to that seen in the section for inclination. First, a comparison of ACO mean motion vs. predicted (TLE) mean motion is shown in Figure 13, and a more concise range of mean motions using the same data is shown in Figure 14. The data shown in Figure 13 center around the mean motion of 1, which is to be expected. Some of the data fall above and below these data, meaning the data were collected on both sub-synchronous and super-synchronous GEO objects. Figure 14, in which the data are shown in a more concise range of values, shows a straight line through a predicted value of 1.0027 revs/day, but that value has a range of possible values for the ACO mean motion. No reason can be found to explain the results. Although this looks like a large error, by examining the range in values it is seen that this error is very small.

The data in Figure 15 show the error in mean motion vs. the ACO mean motion. The spread in the error is spaced equally between negative and positive values in error. However, there is a slight slope from the upper left to the lower right seen, specifically, in both sets of data. This was also seen in the 2002–2003 data and the 2004-2006 data, and no reason for this slope could be obtained.

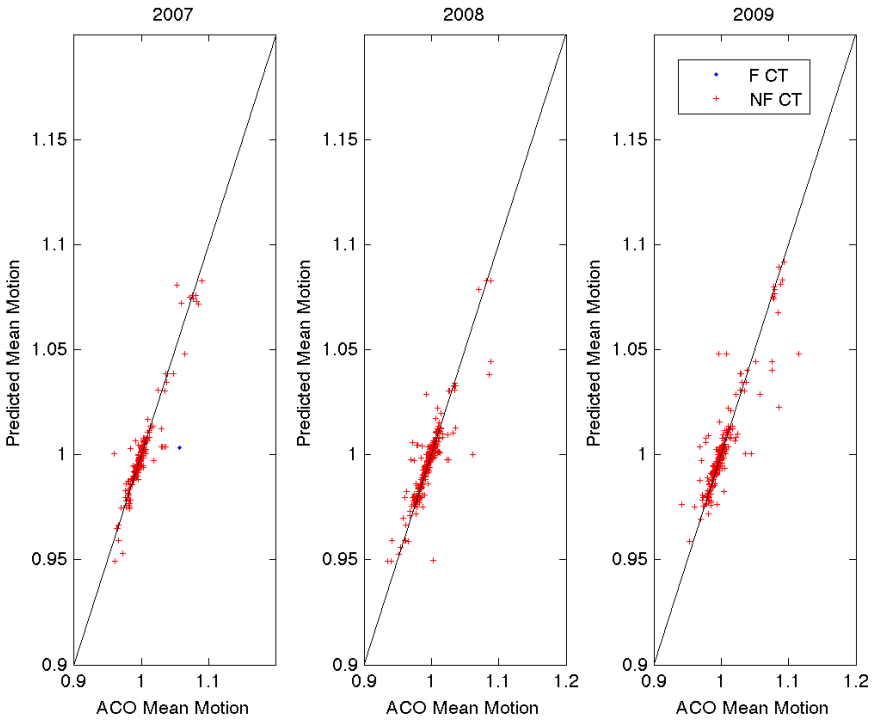

Figure 13. Comparison of inferred and known mean motion.

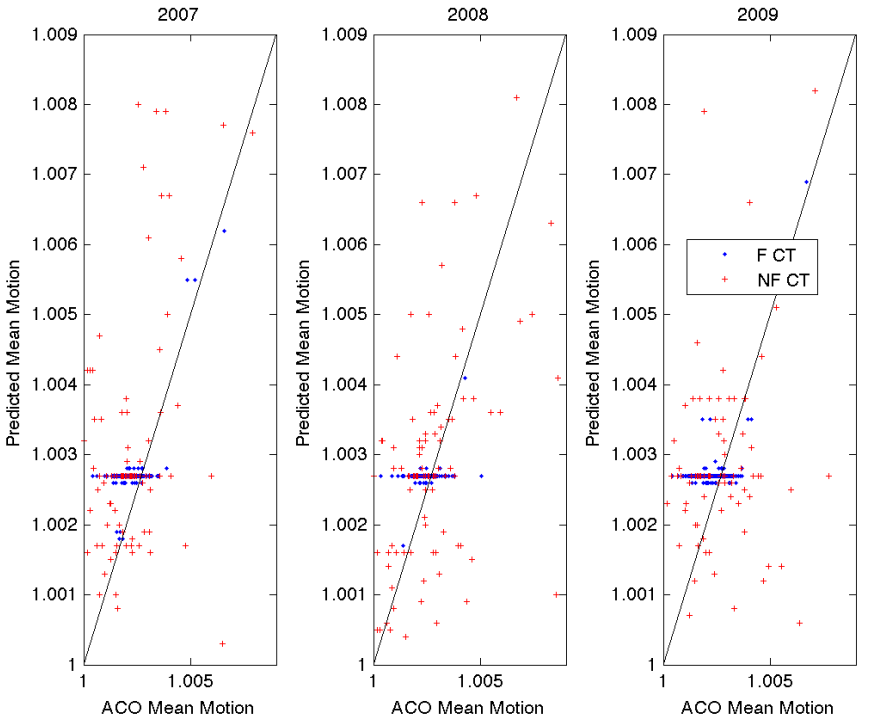

Figure 14. Comparison of inferred and known mean motion, concise range.

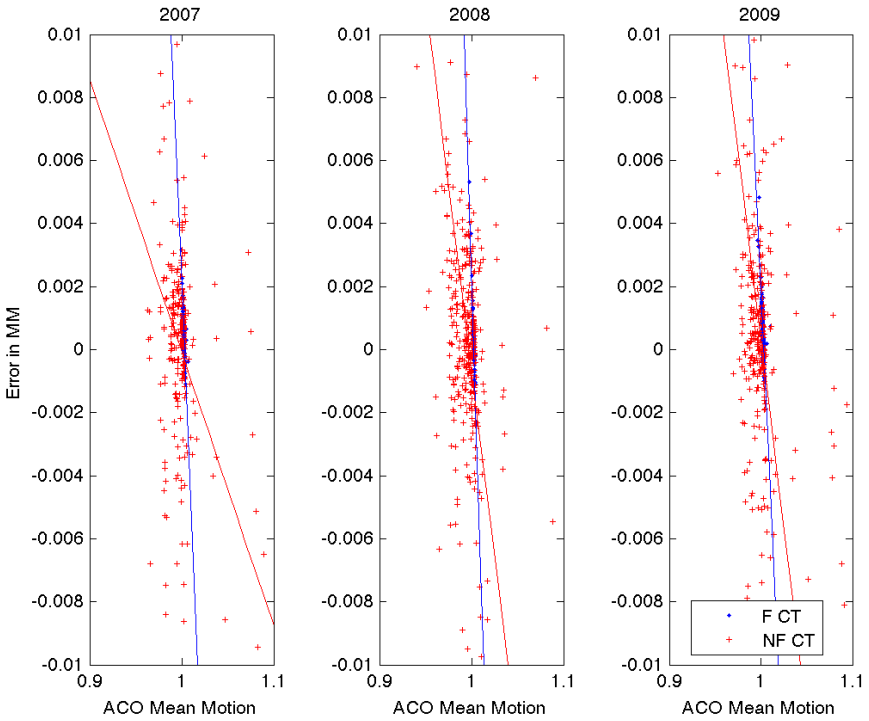

Figure 15. Mean motion error vs. ACO mean motion. Solid lines are the slopes associated with the data.

3.5.3.3 RAAN Determination

The calculation of RAAN is very difficult to determine accurately when the INC of the orbit is near 0°. Therefore, a breakdown of the data is shown for all objects and then for objects with calculated INCs greater than 1°. The latter case is one thought to be more like debris. RMS error data for RAAN are shown in Table 3. In this table, there are 332 functional objects, 28 functional objects with large inclinations, and 236 non-functional objects in 2007; 192 functional objects, 35 functional objects with large inclinations, and 376 non-functional objects in 2008; and 829 functional objects, 69 functional objects with large inclinations, and 310 non-functional objects in 2009. As shown, the largest error occurs when objects with less than 1° INC are included. Once those are removed, the error is much smaller and is similar in order to the error seen with nonfunctional objects. This makes sense as most nonfunctional objects will have INCs greater than 1°.

Table 3. RAAN Errors

Type of Error (reported in degrees)	Functional objects	Functional Objects INCs > 1°	Non-functional objects
RMS 2007	73	23	2
RMS 2008	72	13	1
RMS 2009	86	10	1

The data shown in Figure 16 are for the calculated RAAN vs. predicted RAAN. Here it is shown clearly that the RAAN calculation for functional CTs, which nominally have 0° inclination, are erroneous. Nonfunctional CTs have good agreement with the predicted value of RAAN, showing that the calculation of RAAN is a valid calculation.

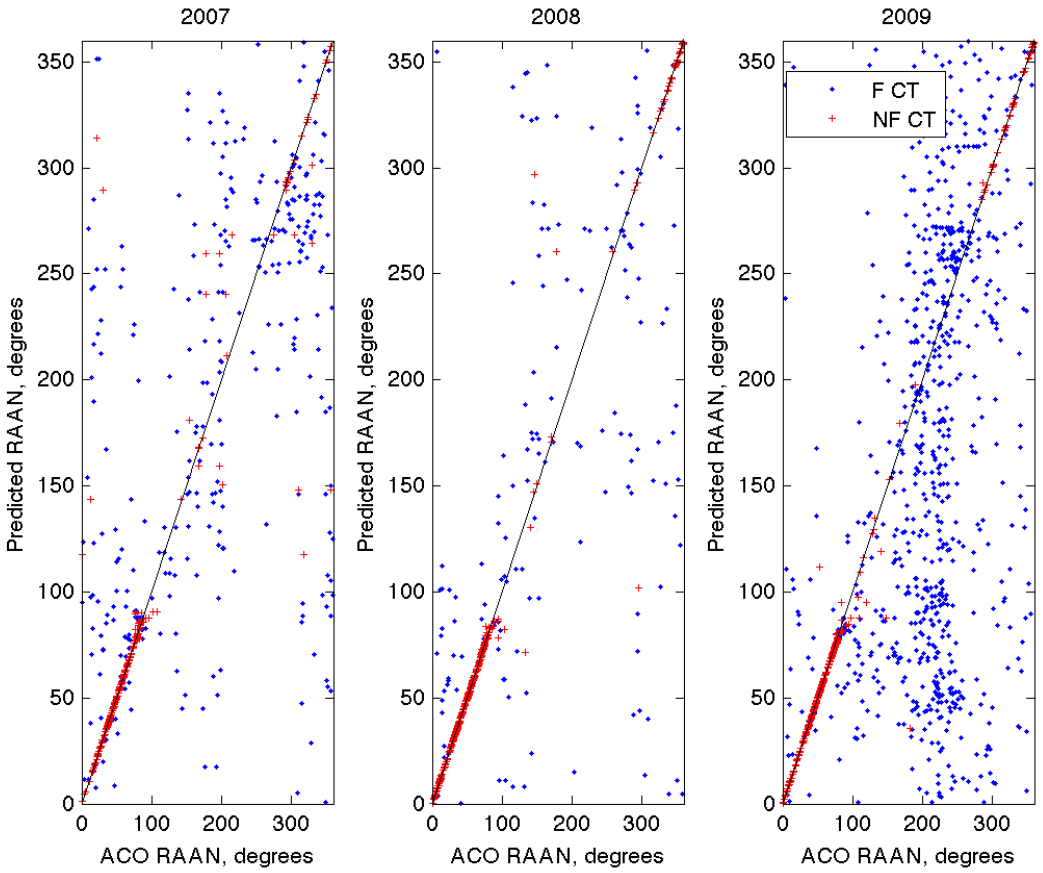

Figure 16. Comparison of inferred and known RAAN.

Figure 17 shows the error in the RAAN calculation compared to the ACO INC. Notice that objects with large errors are associated with very small INCs and those errors are usually CT objects. Some interesting structure arises when the same plot is focused on the smaller errors, as shown in Figure 18. In both the 2007-2009 and the 2002–2003 data sets, the data show two sets of arcs seen in the nonfunctional CT data both above and below the zero error line. However, the 2004–2006 data show only one of the arcs, the one stemming from below the zero line. Objects found along this arc do not have anything in common in regards to date of collection, time of year, object number, or eccentricity. The only factor they have in common is that the lower the INC, the higher the error. It appears, however, that the RAAN results are slightly underdetermined; therefore, underdetermining lessens as RAAN increases.

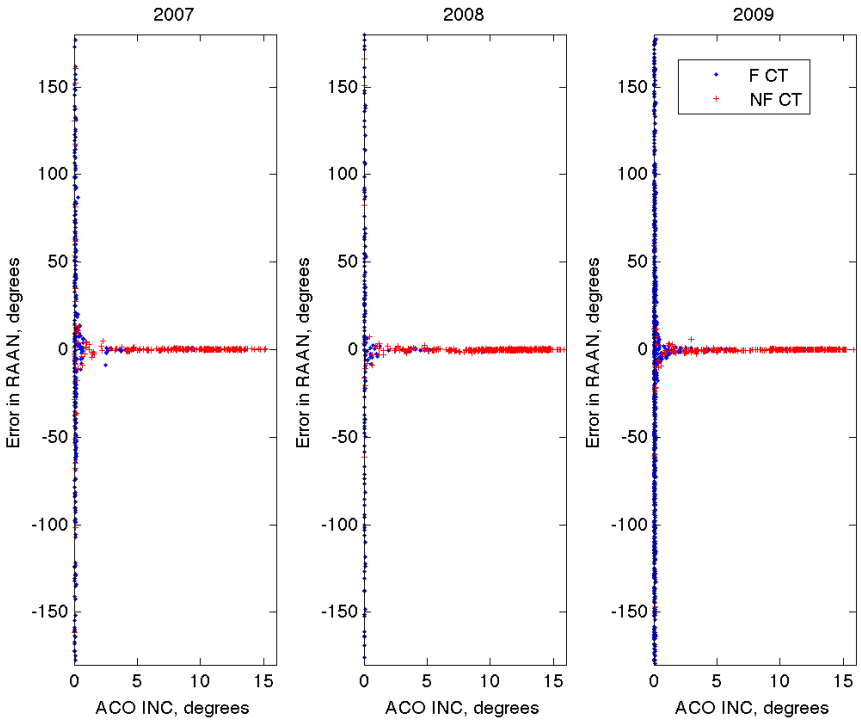

Figure 17. RAAN error as a function of INC (focus on larger errors).

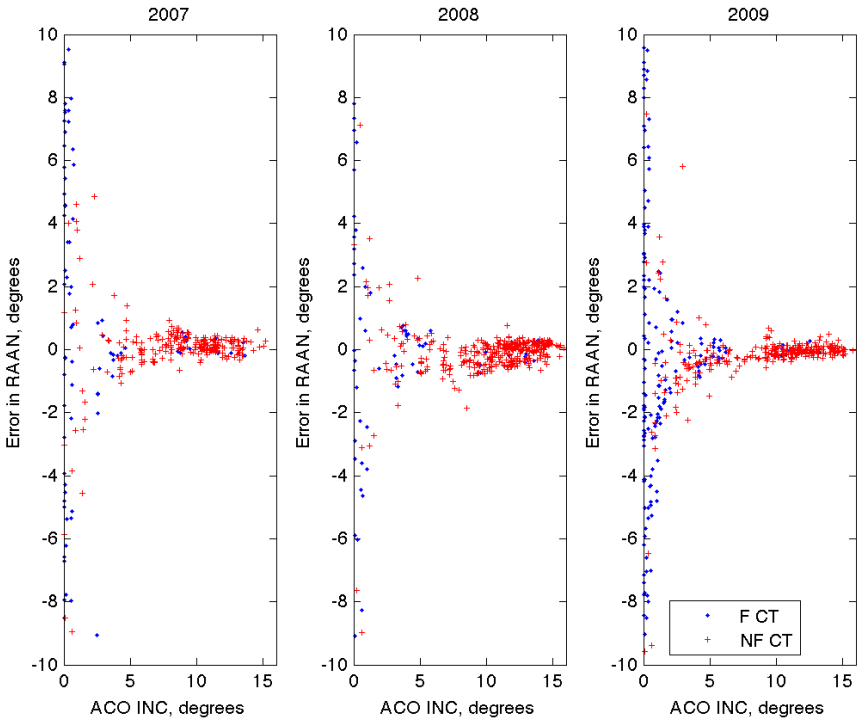

Figure 18. RAAN error as a function of INC (focus on smaller errors).

3.6 Summary of Data Processing

Once the data are collected, the subsequent processing steps performed are as follows:

1) Objects are identified as either CTs or UCTs.
2) Orbital elements (INC, range, RAAN, mean motion) for CTs are calculated from circular orbit fits, and biases or errors are determined to be applied to the UCT elements
3) Sizes of detected objects are estimated, assuming an average albedo of 0.175 and Lambertian phase function.
4) Probability of detection, defined as the likelihood of detection in a given orbit, is calculated based on the location of the telescope at a given time and date.

4.0 Results

4.1 Detection Rates

Thirty-six nights of data were reduced for CY 2007, starting with day of year (DOY) 071 and ending with DOY 320. For CY 2008, 43 nights of data were reduced, starting with DOY 036 and ending with DOY 305. In CY 2009, 43 nights of data were reduced, starting with DOY 025 and ending with DOY 322. In Table 4, the data collected are categorized by observing year. For each year, the percentage of CTs and UCTs observed, the average number of CTs and UCTs detected each night for all locations, and the average number of CTs and UCTs detected per night, when not on the GEO belt, are shown; i.e., for those objects with INCs <1°. The GEO belt is the nominal location of spacecraft that are being station-kept. Most of the objects in this regime are CTs; this is shown by the larger decrease in average number of objects collected for the CTs vs. the UCTs.

Table 4. Statistics Data Collection

Year	% CTs	% UCTS	Avg. # of CTs each night	Avg. # of UCTs each night	Avg. # of CTs – no belt	Avg. # of UCTs – no belt
2007	75%	24%	17	6	10	5
2008	66%	34%	14	7	11	7
2009	82%	18%	27	6	10	9

4.2 Location of Field Centers and Detections

During a normal 2-week telescope run, the strategy is to keep the RA unchanged while offsetting in DEC by ±1.2 degrees each night. In addition, the RA was chosen based on the location of the anti-solar point and the closest proximity to that point possible without being in the shadow of the Earth. The data in Figure 19 shows, using dots, a snapshot view of where objects are expected to be located given an RA and a DEC. These data are a snapshot of DOY 365 for 2003. The overall view of the plot will be similar regardless of the day used. The near-solid line of dots near 5° DEC is the location of the GEO belt as seen from CTIO. The red squares show the observing location of the telescope for each night in 2007, the blue squares show the locations for each night in 2008, and the green squares show the locations for each night in 2009. Overlapping of field locations on different years occurs often, when looking at the belt, and for one run in 2008 and 2009 near 9 hours RA. These data show that coverage of the possible RAs and DECs is enhanced by looking beyond where objects are expected to be to areas where no objects are predicted. Please note, the size of the square on the plot does not depict the size of the FOV for the telescope.

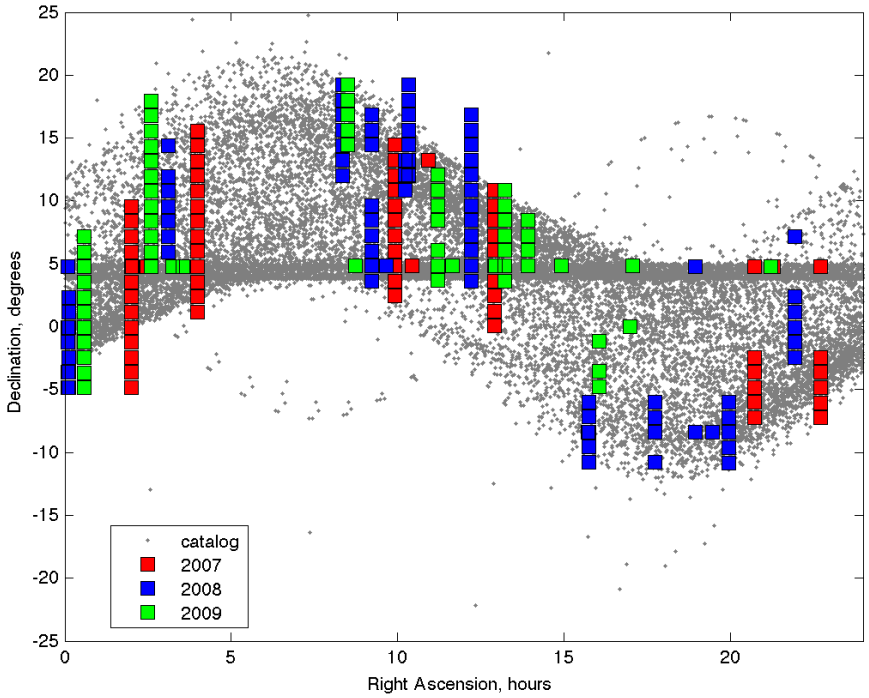

Figure 19. Location of field centers.

Once the field centers are determined, the data are run through a code that determines the probability of detecting an object in a specific orbit while at that FOV and at a specific given time. A probability chart is shown in Figure 20. The different colors represent the probability of detection. The redder the color or the closer the probability is to 1, the greater the likelihood an object in that orbit was detected. Overlaid on the probability chart are the actual detections for the 3 years of data; CTs are solid diamonds and UCTs are open circles. Notice that most of the objects detected were in the red region of probability, which means it is likely that all objects in that region were detected. Once the probability chart was created, it was determined that in future telescope runs, FOV locations could be predetermined by filling in areas of the probability chart. Through collecting a larger number of nights, it is possible to assess a population from these probability data.

Figure 21 shows the population prediction based on where and when the telescope looked for objects and where the objects were found. Each object is given a weight that depicts how many times that object should be counted for a statistical sampling of the data. This weight is the inverse of the number of times a random object in that orbit would be expected to be observed. For instance, an object in the GEO belt could be expected (on average) to be observed multiple times over a set of observation runs. Its weighting would, therefore, be less than one. This procedure statistically removes multiple observations of the same object. At the other extreme, there are orbits that have a probability of less than one of detecting an object in them due to the observation times and pointing directions. The weighting of an object in such an orbit would be greater than one, indicating that each object seen is a sample from a larger, undetected population. This method can be statistically extrapolated to estimate the unseen population.

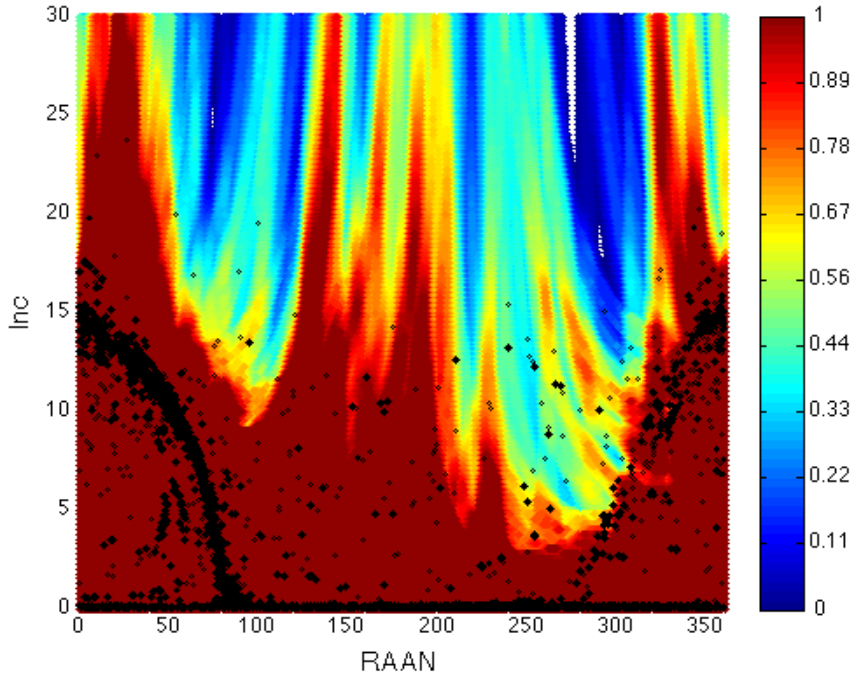

Figure 20. Probability of finding specific orbits based on field center locations during 2007–2009.

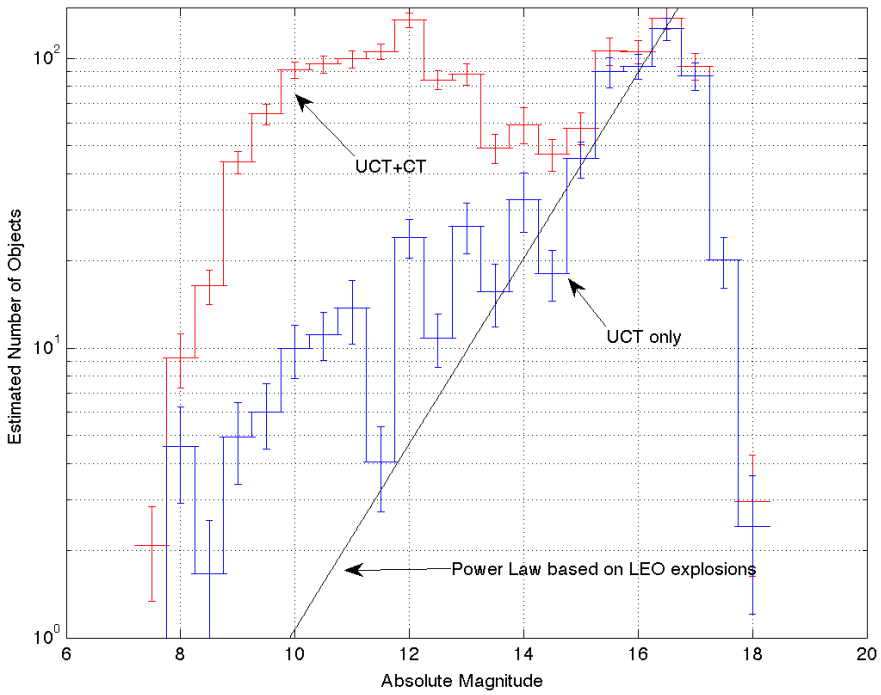

Figure 21. Possible population of UCTs and CTs based on statistical sampling.

Note that Figure 21 also shows the UCTs and CTs combined in one line as well as the UCTs alone for all 2007-2009 data. The objects are binned by absolute magnitude. The error bars are a statistical estimation. The power law distribution for explosions in LEO is plotted with these data.[9] Aligning this power law

distribution line with the UCT data suggests that, if it were not for the fall off in detections due to the telescope size, UCT objects would continue to be found at the rate the black line suggests. Please note that the line should only be compared when the UCT population dominates the CT population at greater than 14th magnitude and noting, as well, that the fall off in detections on the faint end is due to system detection limitations. This analysis is purely statistical, but shows a valuable result of the continuing increase of the number of UCTs as absolute magnitude increases and size decreases. Similar data has been seen in the previous MODEST reports.[10,11]

4.3 Angular Momentum Vector

As previously discussed in Section 3.2, the orbits of GEO and near-GEO objects undergo precession under the influence of Earth's oblateness and the gravity of the sun and the moon. As this precession occurs, the ascending node also precesses such that, to the first order for "perfect" GEO objects, there is a one-to-one correspondence of INC to ascending node. A simple formula to show this relationship between INC *i* and RAAN is given by

$$Cos(i) \approx \frac{1-[x\ Cos(RAAN)]^2}{1+[x\ Cos(RAAN)]^2}$$

where

$$x = \frac{Sin(7.5^\circ)}{Cos(7.5^\circ)}.$$

This behavior can best be seen by the path of the angular momentum vector of the orbit, which traces an arc during this precession cycle centered about a line tilted 7.5° with respect to north pole, as shown in Figure 22. An easy way to show the angular momentum vector for measured objects is to plot the orbital data in a polar graph with the ascending node as the polar angle and the INC as the radius.

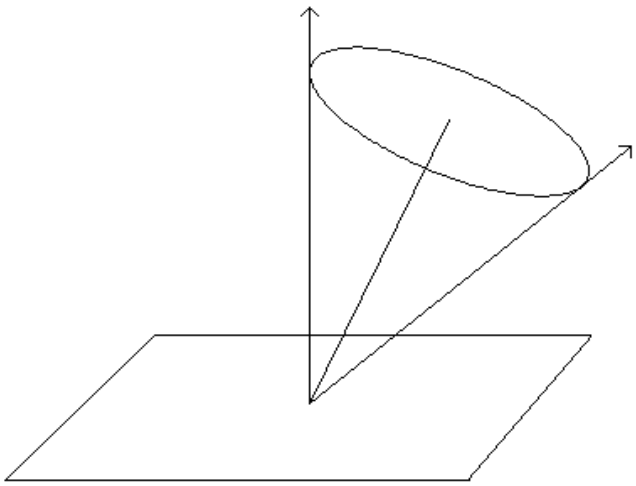

Figure 22. Angular momentum vector of an orbit.

In Cartesian terms,

$$x = i\ Cos(RAAN)$$
$$y = i\ Sin(RAAN).$$

In these coordinates, the path traced out during the precession cycle is a loop. Objects found to reside on or near this idealized loop represent GEO or near-GEO objects at various stages in their orbital evolution. Debris from energetic breakups may stray farther from this idealized path, depending on how strong the delta-velocity was that they received at breakup.

Data collected in CY 2007, CY 2008, and CY 2009 are shown in Figure 23, Figure 24, and Figure 25, respectively. The plot has four subplots, which are termed polar plots due to the coordinate system shown. The upper left image shows only the functional CTs as red solid circles. One can see the data clustering around X = 0 and Y = 0. This was an expected result. The next two subplots show the nonfunctional CTs and the UCTs as blue open circles and green open circles, respectively. The data in these subplots show similar trends of the progression in orbital evolution or perturbations. The UCT data are more scattered; one theory being explored is that the solar radiation pressure is affecting these objects more than the nonfunctional CTs due to size and mass. Once all the data are plotted together, there appears to be an inner circle of data in all three data types. The data shown for all 3 years have similar trends.

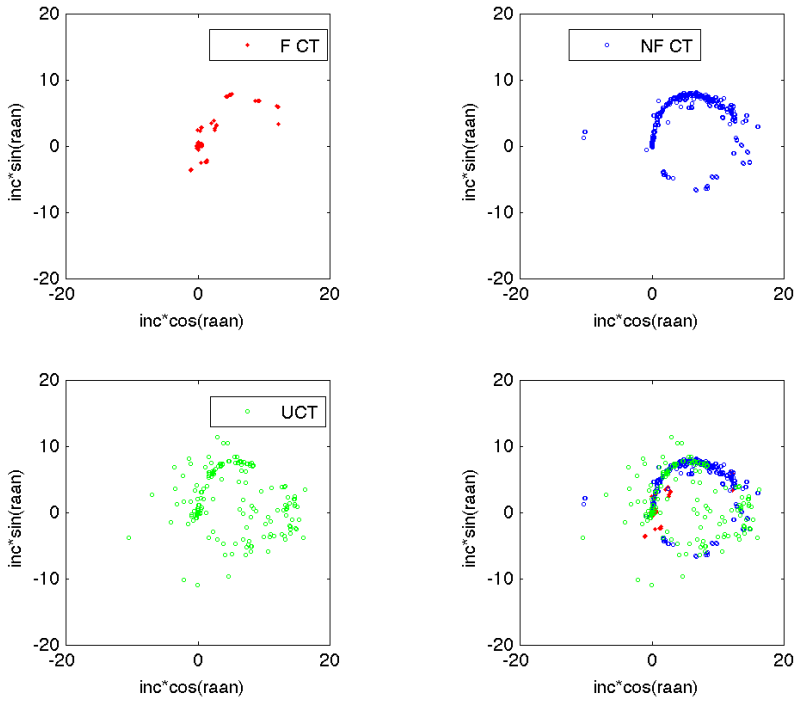

Figure 23. Polar coordinates for objects, CY 2007.

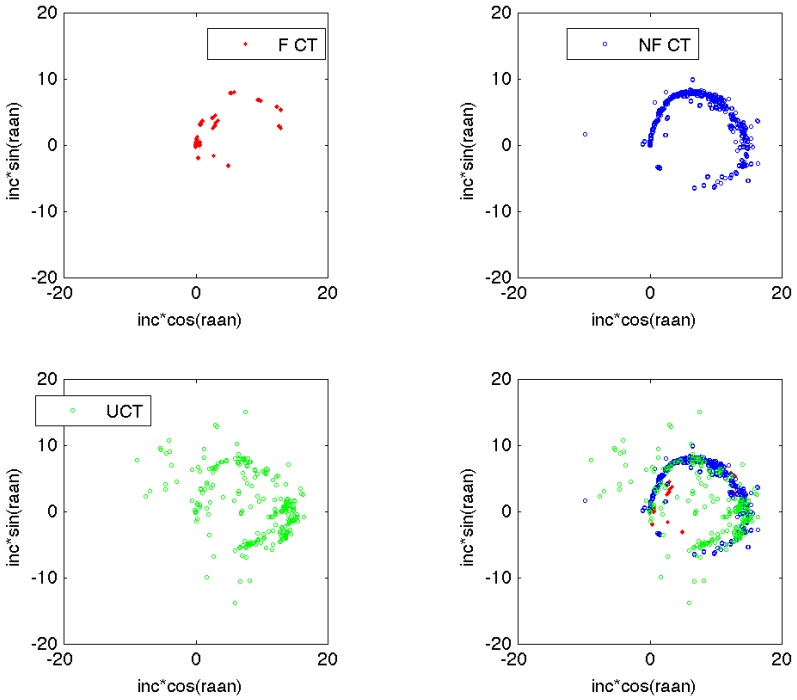

Figure 24. Polar coordinates for objects, CY 2008.

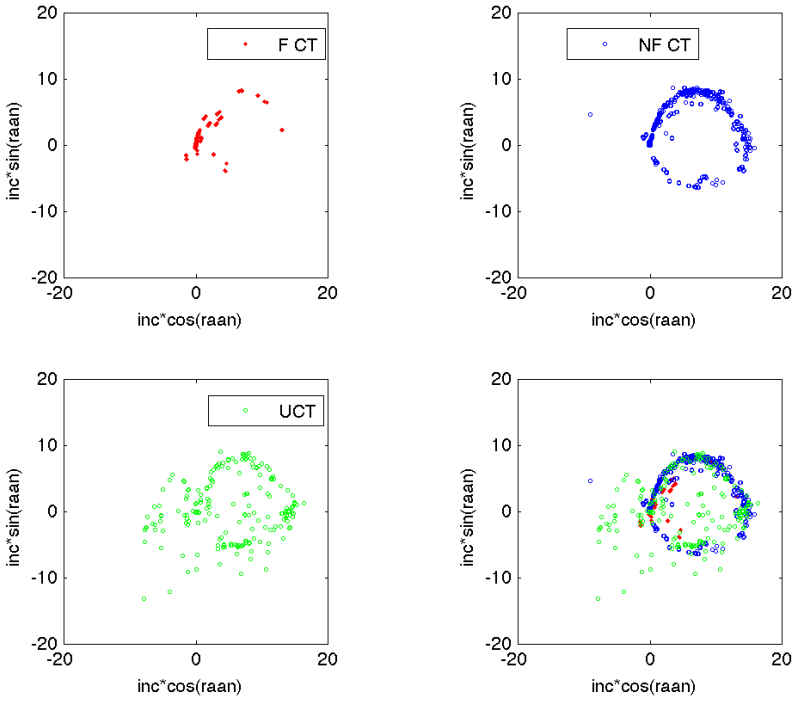

Figure 25. Polar coordinates for objects, CY 2009.

Figure 26 shows the probability of detection data converted into polar data and overlaid with detections. This type of data is helpful both to show a completion of coverage lending credence to where the next observing run should focus and to determine whether initial observations are in the right place.

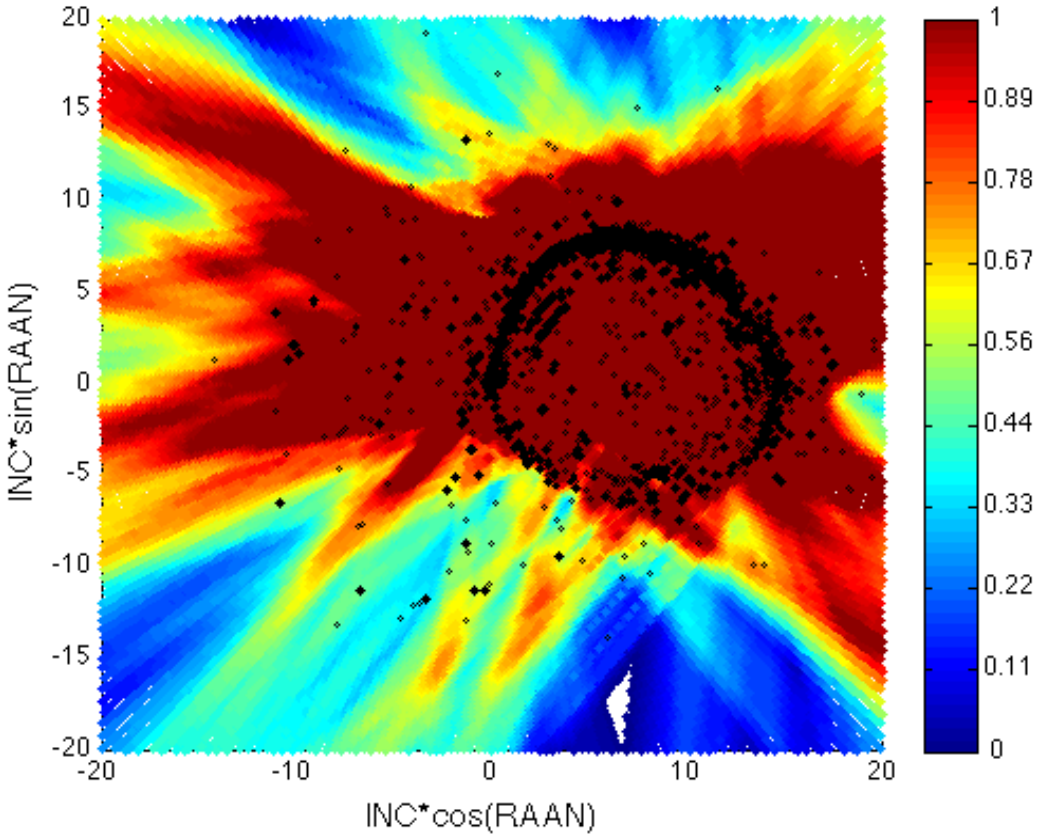

Figure 26. Polar coordinates with probability and detections overlaid for all 2007–2009 data. The CTs are solid diamonds and the UCTs are open diamonds.

4.4 No-sees

Data reduction includes predicting which known satellites from the U.S. SSN catalog will be seen in which observational frame. If a satellite is predicted to be present but evidence for its presence is not found, it is listed as a "no-see." There are multiple potential reasons for an object's non-detection, such as having too faint a visual magnitude or being outside of the rate box. It is important to understand why an object is not seen as this aids in our understanding of the debris environment and determining the limits of this method of analysis. Lack of detection of an object does not necessarily mean the object is not present; it can as easily indicate changes in the orbital elements, a breakup, or even changes in orientation. A detailed no-see analysis was completed for the 2002–2003 data, and it is not believed that the results differ for this set of data. Refer to the 2002–2003 report for more details.[10]

4.5 Mean Motion Distribution

The mean motion of most GEO objects is very close to 1 rev/day. The actual value usually seen for functional CTs in the TLEs shows a value closer to 1.0027 revs/day. Figure 27 compares mean motions for functional and nonfunctional CTs and UCTs. As expected, the large percentage of functional CTs is seen near a mean motion of 1 (98 % of the objects). In addition, a large percentage of the nonfunctional CTs is also seen near 1 (45% of the objects collected). However, there are more nonfunctional CTs spread

throughout the various mean motions, similar to that of the UCTs. The UCTs have the highest percentage of objects near 1 rev/day at 15% and 0.9 rev/day at 15%. UCTs, unlike non-functional CTs and functional CTs, are also seen at mean motions as small as 0.9 and as high as 1.08. Because of this variance, it is believed the ACO calculation is inducing an error into the calculation of mean motion for these objects.

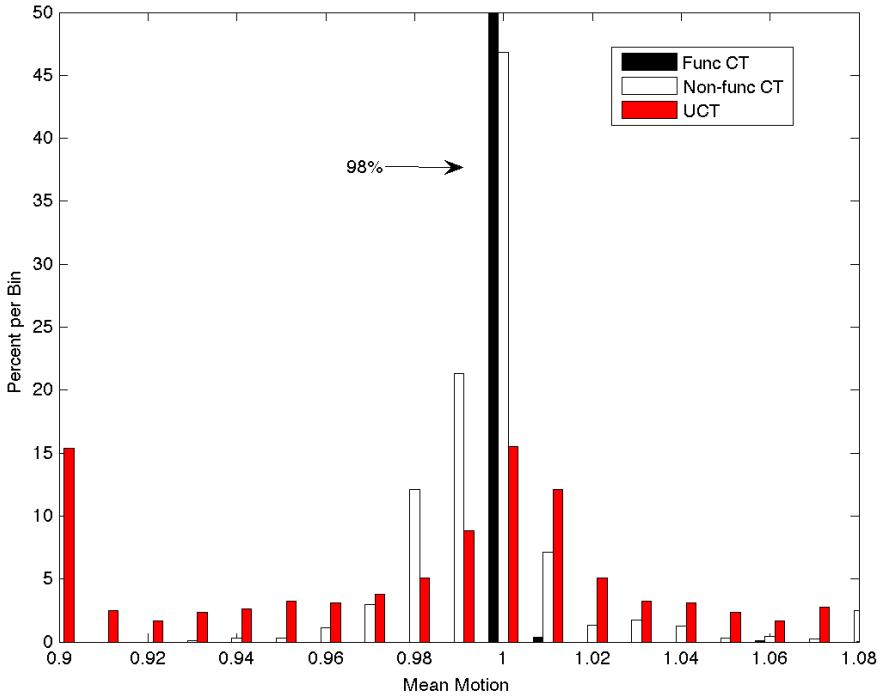

Figure 27. Mean motion distribution for CT and UCT objects.

4.6 Inclination Distribution

As expected, the INC distribution for functional CTs aligns with near 0° INC, with 87% of the detected objects showing in that bin, as shown in Figure 28. Nonfunctional CTs are seen through all INC bins up to 15° to 16°, as is expected due to the propagation of INC with orbital age (see Section 3.2 for a detailed discussion). The UCTs have a similar spread in INC bins. In the 2002–2003 data, two peaks were located near 6° and 12° INC. This does not seem to be the case for the 2004–2006 data. One could argue a peak near 11° INC, but there was no evidence to support the two peaks seen in previous years. The 2007-2009 data show a drop in the number of objects at 12° and 13°, which would imply a peak at 11° and 14° INC. The nonfunctional CTs seem to peak at 12° INC, exactly where the UCTs are lacking data. The indication of a peak in the UCT data could signal the location of a breakup; however, clustering is easier to see when a comparison of INC versus RAAN is calculated. Those data are shown in Section 4.9.

4.7 RAAN Distribution

The distribution of RAAN in the functional CT, nonfunctional CT, and UCT populations is shown in Figure 29. One peak in the UCTs is seen located near 350°. There is a general increase in the number of objects seen from 0-90° and 330-360°. Previous data sets have shown only two peaks, near 80° and near 330° locations. In previous years' reports, no peak is seen with the nonfunctional CTs near 80°, a similar location to that of one of the two UCT peaks. These data show a nonfunctional CT peak at 50°. The difference for the data is unknown at this time. Peaks in functional data are not discussed since most of the objects that are functional are kept near 0° INC, leading to an erroneous RAAN.

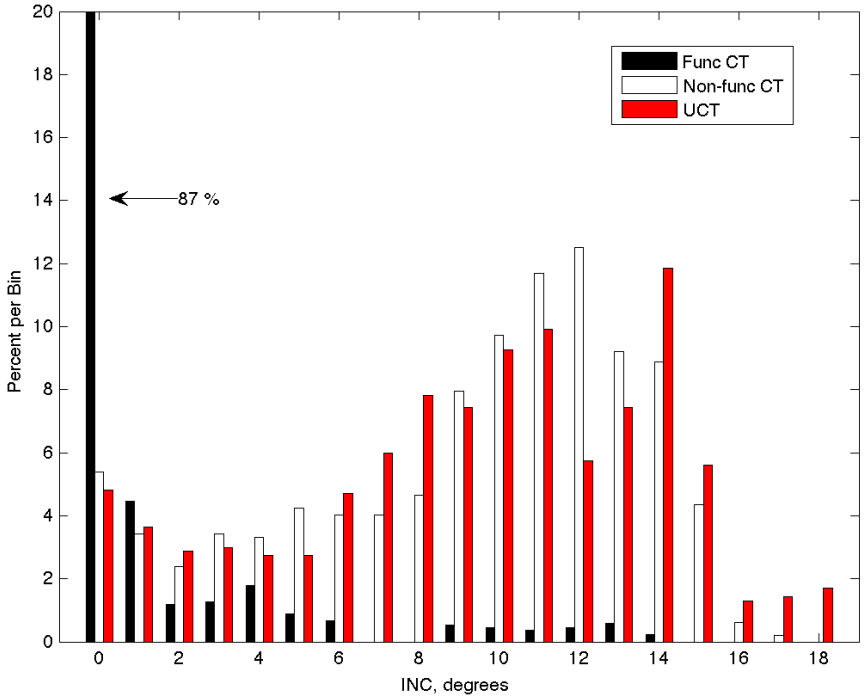

Figure 28. Distribution of INC for CTs and UCTs.

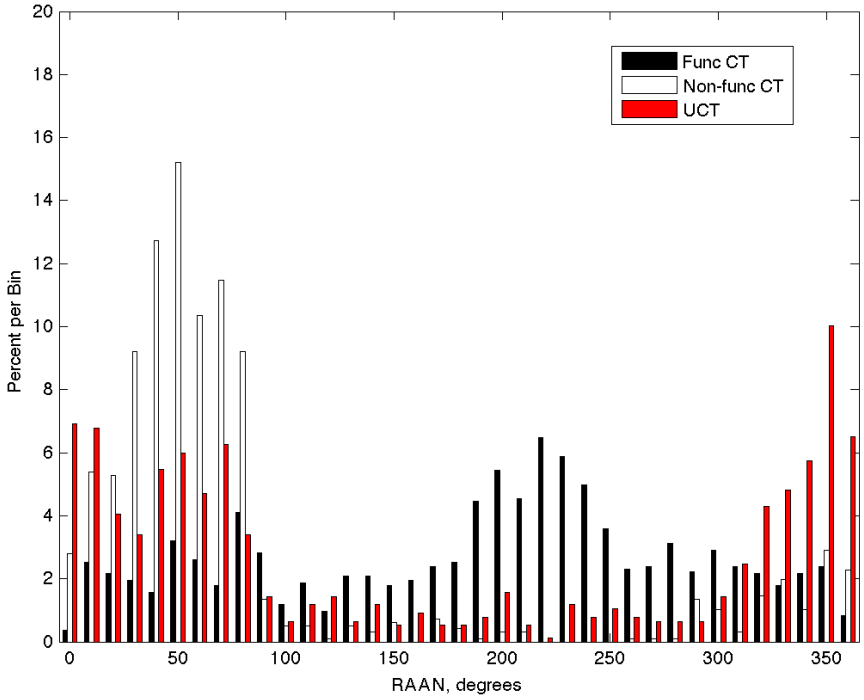

Figure 29. Distribution of RAAN for CT and UCT. The location of the data found is biased by the field center selection and the DOY.

4.8 Absolute Magnitude Distribution and Derived Diameters

As discussed in previous sections, the derived diameters stem from assuming an albedo of 0.175 and a diffuse Lambertian phase function.[6] A mean distance of 36,000 km is also used. As a reminder, the absolute magnitude is a log calculation (unitless); the smaller the number, the brighter and, likely, larger the object. The distribution of absolute magnitudes is shown in Figure 30. Overlaid on the distribution are the diameters associated with a few of the bins. The peak in absolute magnitude for functional CTs is seen at 10.5, corresponding to a size of 6.3 m. The peak of the nonfunctional objects is seen near 12.5, which is a size of 2.5 m. The catalog is said to be complete down to 1 m at GEO; using the assumptions above, this corresponds to an absolute magnitude of 14.4. The peak of the UCTs is an artificial one due to the detection capabilities of the telescope. It is believed, due to the statistical data shown in Section 4.2, that the UCT population will continue on the same slope throughout the fainter magnitudes. The smallest detected object to be seen with MODEST during this reporting period is 18.3 magnitude, converted to 17 cm using the albedo and phase function assumptions.[6]

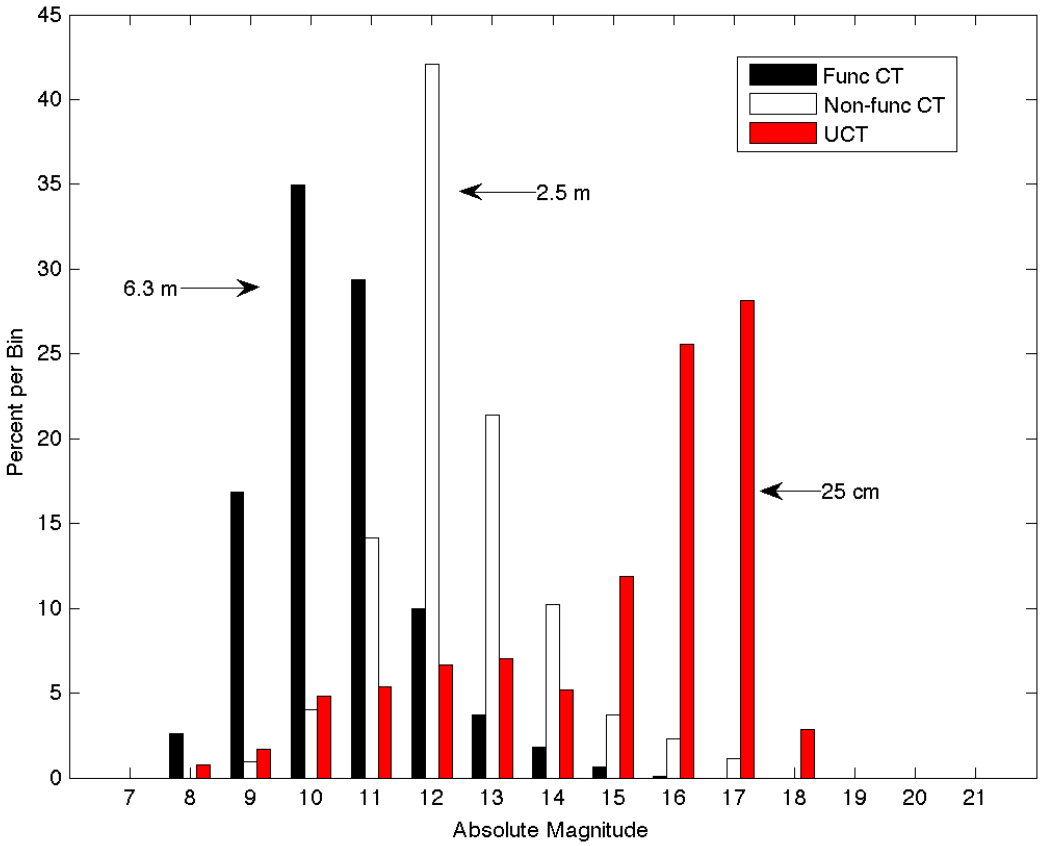

Figure 30. Absolute magnitude and derived size distribution, assuming an albedo of 0.175 and a diffuse Lambertian phase function.

4.9 RAAN vs. INC Distribution

The INC and RAAN distributions for the detected objects are shown in Figure 31. The top figure shows the data collected in 2007, the middle figure the 2008 data, and the bottom figure the data collected in 2009. The data show a collection of UCTs near 330° RAAN and 10° INC. This first clumping is believed to be the location of the Titan breakup, discussed in Section 2.0. Similar clustering is seen near 350-360° RAAN, 14° INC and 0-10° RAAN, 14° INC. However, as no known breakups have occurred in

that area, the clusters may indicate locations of unknown breakups. More data need to be collected to confirm these findings. The data in these plots show the expected climb toward 15° INC for the UCTs and nonfunctional CTs as well as for the functional CTs at various RAANs with 0° INC. Figure presents all the data together. The two clusters of UCTs are still visible. The 2004-2006 data show three clusters and the third was near 70° RAAN and 5° INC.[11] This cluster is not seen in the data.

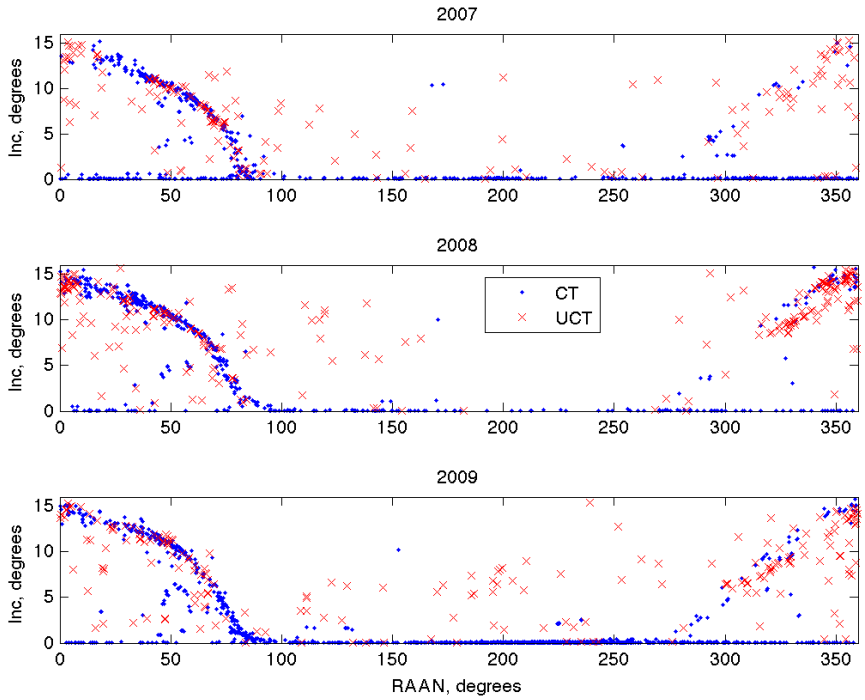

Figure 31. RAAN vs. INC for CT and UCT objects.

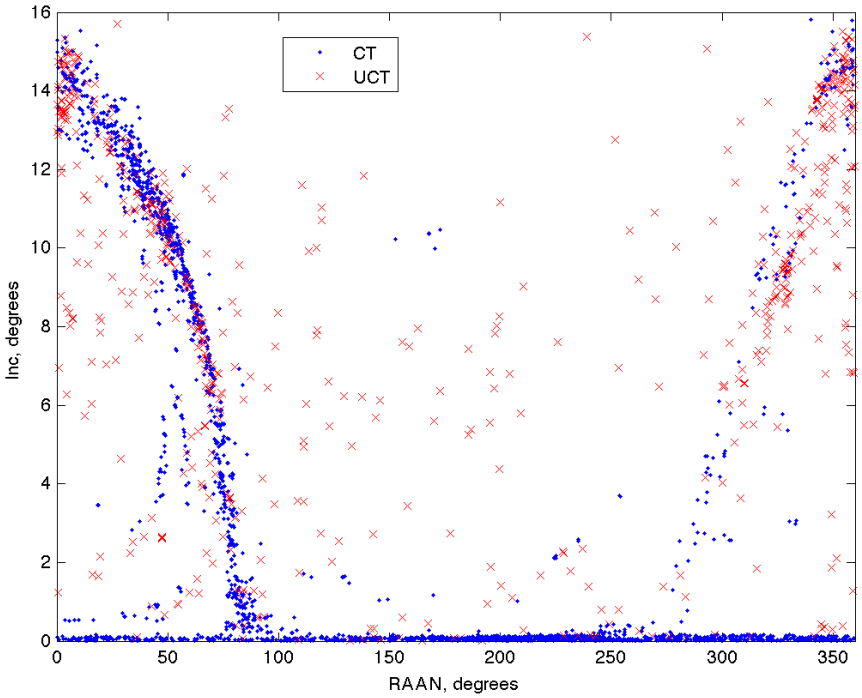

Figure 32. RAAN vs. INC for CT and UCT data for all 3 years.

5.0 Conclusions

This JSC report provides details of observational and data-reduction processes for the entire MODEST dataset acquired in CYs 2007, 2008, and 2009. Specifically, this report describes the collection and analysis of 36 nights of data collected in CY 2007, 43 nights of data collected in CY 2008, and 43 nights of data collected in CY 2009.

The average number of detections each night over all 3 years was 26. On average in CY 2007, 75% of the detections were CTs and 25% were UCTs; in CY 2008, 66% of the detections were CTs and 34% were UCTs; and in 2009, 82% of the detections were CTs and 18% were UCTs. This variation in percentages between the years may be due to observations that were made in different locations with respect to the GEO belt.

Errors associated with the calculated quantities of range, INC, and RAAN were derived by comparing values calculated using an ACO and those known values seen in the TLE. The average INC RMS error is 0.05° for both functional CTs and nonfunctional CTs. Due to the fact that RAAN is ill-defined at values near 0° INC, the RMS error for RAAN is calculated only for objects with an INC greater than 1°. The average RAAN RMS error is 10° for functional objects and 15° for nonfunctional objects in CY 2007; 8° for functional objects and 5° for nonfunctional objects in CY 2008; and 12° for both functional and for nonfunctional objects in CY 2009. The mean motion error is 0.0034 for functional objects and 0.062 for nonfunctional objects in CY 2007; 0.001 for functional objects and 0.008 for nonfunctional objects in CY 2008; and 0.002 for functional CTs and 0.010 for nonfunctional CTs in CY 2009. This error analysis of CT values for INC, RAAN, and mean motion lends credibility to the determination of the UCT orbital distributions.

The distribution of objects found UCTs clustering in two locations, with only one corresponding to a known breakup, namely the breakup of Titan. More data are needed to confirm whether the other clusters represent unknown breakups.

The absolute magnitude distribution showed a peak for the functional CTs at 10^{th} magnitude. An absolute magnitude of 10.5 corresponds to objects having average diameters of 6 m, assuming an albedo of 0.175 and a diffuse Lambertian phase function. This result generally agrees with the known sizes of intact satellites. The absolute magnitude distribution for the UCTs is broad, but starts to roll off near a diameter of 25 cm or 17.5 magnitude. The roll off in the distribution reflects the detection capability of MODEST and does not reflect the true nature of the population. The true population is believed to continue at the same slope through fainter magnitudes, as was shown when the statistical population was compared to the power-law distribution of low-Earth orbit breakups.

6.0 References

[1]Johnson, N.L., et al. “History of On-Orbit Satellite Fragmentations.” *JSC-29517*, Houston, TX, 2001.

[2]Pensa, A. F., et al. “Debris in Geosynchronous Orbit.” *SPACE FORUM*, Vol. 1, pp. 23 – 27, 1996.

[3]Talent, D. L. et al. “A Search for Debris in GEO.” *Proceedings of the Second European Conference on Space Debris*, Darmstadt, Germany, 1997.

[4]Friesen, L. et al. “Results in Orbital Evolution of Objects in the Geosynchronous Region.” AIAA 90-1362, *AIAA/NASA/DOD Orbital Debris Conference: Technical Issues and Future Directions*, Baltimore, MD, 1990.

[5]Vaughan, S. H. and Mullikin, T. L. “Long Term Behavior of Inactive Satellites and Debris Near Geosynchronous Orbits.” AIAA 95-200, *AAS/AIAA Spaceflight Mechanics Meeting*, Albuquerque, NM, 1995.

[6]Mulrooney, M.K., Matney, M.J., and Barker, E.S. “A New Bond Albedo for Performing Orbital Debris Brightness to Size Transformations.” *International Astronautical Congress*, Glasgow, Scotland, 2008.

[7]Press, W.H., Teukolsky, S.A, Vetterling, W.T., and Flannery, B.P. *Numerical Recipes in Fortran 90*. Cambridge University Press. Volume 2. January 1996.

[8]Hoots, F.R. and Roehrich, R.L. “Spacetrack Report #3: Models for Propagation of the NORAD Element Sets.” U.S. Air Force Aerospace Defense Command, Colorado Springs, CO.

[9]Johnson, N.L., Krisko, P.H., Liou, J.C., Anz-Meador, P.D.: “NASA’s New Breakup Model of EVOLVE 4.0.”, *Adv. Space Res.*, Vol. 28, No. 9, pp 1377-1384, 2001.

[10]Abercromby, K.J., Seitzer, P., Barker, E.S., Cowardin, H.M., Matney, M.J., Parr-Thumm, T.L. "Michigan Orbital DEbris Survey Telescope Observations of the Geosynchronous Orbital Debris Environment , Observing Years: 2002–2003." NASA/TP-2010-216128, Houston, TX, 2010.

[11]Abercromby, K.J., Seitzer, P., Barker, E.S., Cowardin, H.M., Matney, M.J., "Michigan Orbital DEbris Survey Telescope Observations of the Geosynchronous Orbital Debris Environment, Observing Years: 2004–2006." NASA/TP-2010-216129, Houston, TX, 2010.

Appendix A:
Fields File Example

(This is a representative sample of the file)

DEC	RA	Time	Frame
4.842	124.306	10368.1	19
4.842	124.306	10406.0	20
4.842	124.306	10443.9	21
4.842	124.306	10481.8	22
4.842	124.306	10519.7	23
4.842	124.306	10557.6	24
4.842	124.306	10595.5	25
4.842	124.306	10633.4	26
4.842	124.306	10671.3	27
4.842	124.306	10709.2	28
4.842	124.306	10747.1	29
4.842	124.306	10785.1	30
4.842	124.306	10822.9	31
4.842	124.306	10860.8	32
4.842	124.306	10898.7	33
4.842	124.306	10936.6	34
4.842	124.306	10974.6	35
4.842	124.306	11012.5	36
4.842	124.306	11050.4	37
4.842	124.306	11088.3	38
4.842	124.306	11126.2	39
4.842	124.306	11164.1	40
4.842	124.306	11202.0	41
4.842	124.306	11239.9	42
4.842	124.306	11277.8	43
4.842	124.306	11315.7	44
4.842	124.306	11353.6	45
4.842	124.306	11391.5	46
4.842	124.306	11429.4	47
4.842	124.306	11467.3	48
4.842	124.306	11505.2	49

Appendix B:
Output File Example

The columns are frame number, RA, DEC, epoch, magnitude, date, and time. Two objects are shown, both with nine detections. This output is what NASA receives from the telescope.

```
2002009.0001  9
  29 123.6621   4.8225 2000.0 11.3 2002-01-09  2.98532
  30 123.8204   4.8225 2000.0 11.3 2002-01-09  2.99585
  31 123.9782   4.8225 2000.0 11.3 2002-01-09  3.00637
  32 124.1370   4.8225 2000.0 11.3 2002-01-09  3.01690
  33 124.2953   4.8232 2000.0 11.3 2002-01-09  3.02743
  34 124.4537   4.8243 2000.0 11.3 2002-01-09  3.03795
  35 124.6126   4.8244 2000.0 11.3 2002-01-09  3.04849
  36 124.7703   4.8244 2000.0 11.3 2002-01-09  3.05902
  37 124.9286   4.8244 2000.0 11.3 2002-01-09  3.06955
2002009.0002  9
  50 123.6602   4.8534 2000.0 11.2 2002-01-09  3.20642
  51 123.8191   4.8534 2000.0 11.2 2002-01-09  3.21695
  52 123.9768   4.8534 2000.0 11.2 2002-01-09  3.22747
  53 124.1358   4.8534 2000.0 11.2 2002-01-09  3.23800
  54 124.2943   4.8543 2000.0 11.0 2002-01-09  3.24853
  55 124.4524   4.8534 2000.0 11.2 2002-01-09  3.25907
  56 124.6103   4.8539 2000.0 11.2 2002-01-09  3.26959
  57 124.7690   4.8553 2000.0 11.2 2002-01-09  3.28012
  58 124.9276   4.8553 2000.0 11.2 2002-01-09  3.29065
```

Appendix C:
Correlation Output

These data are the correlation file for the two objects listed in Appendix B. The computer correlated one object; the other object was correlated by hand.

		newRAoffset	newDECoffset	newsquare	Match	Mag	UT	OMM	OINC	ORAAN	AM	PRANGE	PECC	PINC	PMM	PRAAN
11	1 to 21765	-0.009645	-0.007828	0.012422	CORRELATES	11.3	2.98532	1.00264220	0.0947	117.1440	11.0	37995	0.0000960	0.00	1.0027	8.82
12	1 to 21765	-0.010087	-0.007838	0.012774	CORRELATES	11.3	2.99585	1.00264220	0.0947	117.1440	11.0	37995	0.0000960	0.00	1.0027	8.82
13	1 to 21765	-0.010196	-0.007849	0.012867	CORRELATES	11.3	3.00637	1.00264220	0.0947	117.1440	11.0	37995	0.0000960	0.00	1.0027	8.82
14	1 to 21765	-0.009721	-0.007858	0.012500	CORRELATES	11.3	3.01690	1.00264220	0.0947	117.1440	11.0	37995	0.0000960	0.00	1.0027	8.82
15	1 to 21765	-0.009746	-0.007168	0.012098	CORRELATES	11.3	3.02743	1.00264220	0.0947	117.1440	11.0	37995	0.0000960	0.00	1.0027	8.82
16	1 to 21765	-0.009672	-0.006077	0.011423	CORRELATES	11.3	3.03795	1.00264220	0.0947	117.1440	11.0	37995	0.0000960	0.00	1.0027	8.82
17	1 to 21765	-0.009515	-0.005986	0.011241	CORRELATES	11.3	3.04849	1.00264220	0.0947	117.1440	11.0	37995	0.0000960	0.00	1.0027	8.82
18	1 to 21765	-0.010142	-0.005996	0.011782	CORRELATES	11.3	3.05902	1.00264220	0.0947	117.1440	11.0	37995	0.0000960	0.00	1.0027	8.82
19	1 to 21765	-0.010167	-0.006004	0.011807	CORRELATES	11.3	3.06955	1.00264220	0.0947	117.1440	11.0	37995	0.0000960	0.00	1.0027	8.82
32	2 to 23413	0.050185	0.033890	0.060556		11.2	3.20642	1.00277416	0.0699	111.6942	10.9	37798	0.0001629	0.01	1.0026	182.58
33	2 to 23413	0.050687	0.033860	0.060956		11.2	3.21695	1.00277416	0.0699	111.6942	10.9	37798	0.0001629	0.01	1.0026	182.58
34	2 to 23413	0.049991	0.033830	0.060362		11.2	3.22747	1.00277416	0.0699	111.6942	10.9	37798	0.0001629	0.01	1.0026	182.58
35	2 to 23413	0.050594	0.033800	0.060846		11.2	3.23800	1.00277416	0.0699	111.6942	10.9	37798	0.0001629	0.01	1.0026	182.58
36	2 to 23413	0.050698	0.034669	0.061418		11.0	3.24853	1.00277416	0.0699	111.6942	10.9	37798	0.0001629	0.01	1.0026	182.58
37	2 to 23413	0.050401	0.033739	0.060651		11.2	3.25907	1.00277416	0.0699	111.6942	10.9	37798	0.0001629	0.01	1.0026	182.58
38	2 to 23413	0.049905	0.034209	0.060504		11.2	3.26959	1.00277416	0.0699	111.6942	10.9	37798	0.0001629	0.01	1.0026	182.58
39	2 to 23413	0.050209	0.035580	0.061538		11.2	3.28012	1.00277416	0.0699	111.6942	10.9	37798	0.0001629	0.01	1.0026	182.58
40	2 to 23413	0.050412	0.035549	0.061686		11.2	3.29065	1.00277416	0.0699	111.6942	10.9	37798	0.0001629	0.01	1.0026	182.58

REPORT DOCUMENTATION PAGE	Form Approved OMB No. 0704-0188

1. AGENCY USE ONLY *(Leave Blank)*	2. REPORT DATE	3. REPORT TYPE AND DATES COVERED
	September 2011	NASA Technical Paper

4. TITLE AND SUBTITLE
Michigan Orbital DEbris Survey Telescope Observations of the Geosynchronous Orbital Debris Environment
Observing Years: 2007-2009

5. FUNDING NUMBERS

6. AUTHOR(S)
K.J. Abercromby, P. Seitzer, H.M. Cowardin, E.S. Barker, M.J. Matney

7. PERFORMING ORGANIZATION NAME(S) AND ADDRESS(ES)
Lyndon B. Johnson Space Center
Houston, Texas 77058

8. PERFORMING ORGANIZATION REPORT NUMBERS
S-1112

9. SPONSORING/MONITORING AGENCY NAME(S) AND ADDRESS(ES)
National Aeronautics and Space Administration
Washington, DC 20546-0001

10. SPONSORING/MONITORING AGENCY REPORT NUMBER
TP-2011-217350

11. SUPPLEMENTARY NOTES

12a. DISTRIBUTION/AVAILABILITY STATEMENT
Available from the NASA Center for AeroSpace Information (CASI)
7121 Standard
Hanover, MD 21076-1320 Category: 88

12b. DISTRIBUTION CODE

13. ABSTRACT *(Maximum 200 words)*
Orbital debris is a concern to all nations that use satellites or launch space vehicles. The debris field scattered near Earth's geosynchronous orbit (GEO) poses a threat to anything residing in or passing through the region. To mitigate risk and minimize the debris field's expansion, the environment must be understood. NASA uses the Michigan Orbital DEbris Survey Telescope (MODEST), the University of Michigan's 0.61-m aperture Curtis-Schmidt telescope at the Cerro Tololo Inter-American Observatory in Chile, to help characterize the GEO debris environment. This report describes the collection and analysis of data collected during 36 nights in CY 2007, 43 nights in CY 2008, and 43 nights in CY 2009. For all 3 years, the average number of detections each night was 26. The percentage of this number that represented the UCT population ranged from 34% to 18% depending on the observing strategy and the field center location. The data of interest are brightness distributions, inclination, right ascension of ascending node, and mean motion. Estimates on the error for derived quantities of inclination, right ascension of ascending node, and mean motion can be made from derived and known quantities of correlated objects.

14. SUBJECT TERMS	15. NUMBER OF PAGES	16. PRICE CODE
space debris; geosynchronous orbits; Earth orbital environments; brightness; inclination, orbits; targets; range, orbital position estimation; astronomical telescopes	48	

17. SECURITY CLASSIFICATION OF REPORT	18. SECURITY CLASSIFICATION OF THIS PAGE	19. SECURITY CLASSIFICATION OF ABSTRACT	20. LIMITATION OF ABSTRACT
Unclassified	Unclassified	Unclassified	Unlimited